LA-10608-MS

UC-34A
Issued: February 1986

LA--10608-MS

DE86 008323

Transport Coefficients for Carbon, Hydrogen, and the Organic Mixture C_2H_3

George Rinker

Los Alamos National Laboratory
Los Alamos, New Mexico 87545

TRANSPORT COEFFICIENTS FOR CARBON, HYDROGEN, AND THE ORGANIC MIXTURE C_2H_3

by

George Rinker

ABSTRACT

Electrical and thermal transport coefficients are calculated for amorphous elemental carbon and hydrogen, using the best available systematic theoretical methods. The density range considered is $10^{-3}g/cm^3 \leq \rho \leq 10^6 g/cm^3$ for carbon, and $10^{-4}g/cm^3 \leq \rho \leq 10^5 g/cm^3$ for hydrogen. The temperature range considered is $10^{-2}eV \leq kT \leq 10^4 eV$. Calculational methods include relativistic partial-wave analysis of the extended Ziman theory, and nonrelativistic plane-wave analysis (Born approximation) of the original Ziman theory. Physical models include relativistic Dirac-Fock-Slater and nonrelativistic Thomas-Fermi-Dirac electron-ion potentials, and one-component-plasma ion-ion structure factors. A mixing algorithm is used to obtain approximate transport coefficients for the atomic ratio C_2H_3.

---

1. Methods

The calculational methods used are described in detail elsewhere.[1-5] They are summarized here for quick reference. The Ziman formula for the electrical resistivity η is

$$\eta = -\frac{1}{3\pi\alpha}\frac{\Omega}{Z_i^2}\int_0^\infty d\epsilon \frac{d}{d\epsilon} f_{\beta\mu}(\epsilon) \int_0^{2p} dq\, q^3 S(q)\sigma_\epsilon(q) \quad , \tag{1}$$

where Z_i is the number of free electrons per atom (ionization state), $\Omega = 4\pi r_t^3/3$ is the ionic volume, $f_{\beta\mu}(\epsilon)$ is the Fermi-Dirac distribution function

$$f_{\beta\mu}(\epsilon) = \left[e^{\beta(\epsilon-\mu)} + 1 \right]^{-1} , \qquad (2)$$

$\beta=1/kT$ is the inverse temperature, μ is the chemical potential, $S(q)$ and $\sigma_\epsilon(q)$ are the ionic structure factor and the electron-ion elastic scattering cross section for momentum transfer $q=p'-p$ and incident energy $\epsilon=(p^2+m^2)^{1/2}-m\approx p^2/2m$, and $\alpha\approx 1/137.03604$ is the fine structure constant. As in previous work, we drop factors of $\hbar$ and c and measure all quantities in length or inverse-length units.

The chemical potential μ is determined by the requirement of charge neutrality within the ion sphere:

$$Z = \int_{-\infty}^{\infty} d\epsilon \; f_{\beta\mu}(\epsilon) \; \frac{dN}{d\epsilon} , \qquad (3)$$

where $dN/d\epsilon$ is the calculated electron density of states. With the chemical potential thus determined, the ionization state Z_i is computed from

$$Z_i = \int_0^{\infty} d\epsilon \; f_{\beta\mu}(\epsilon) \; \frac{\Omega}{\pi^2} \; p \; (m + \epsilon) . \qquad (4)$$

This is equivalent to multiplying the ionic volume by the electron density at the boundary.

2. Carbon calculations

The essential physical models involve specification of an electron-ion interaction and an ion-ion structure factor. In general, the electron-ion scattering cross section $\sigma_\epsilon(q)$ and density of states $dN/d\epsilon$ are computed from partial-wave analysis of a model potential. The structure factor is specified independently.

2.1 Electron-ion potentials

These potentials are constructed separately for each temperature and material density of interest. Five examples are shown in Fig. 1.

2.1.1 $V_1(r)$

This is a Thomas-Fermi-Dirac (TFD) potential calculated for ρ=3.98107g/cm^3 and kT=10^{-2}eV. The corresponding value of r_t is 1.06146A.

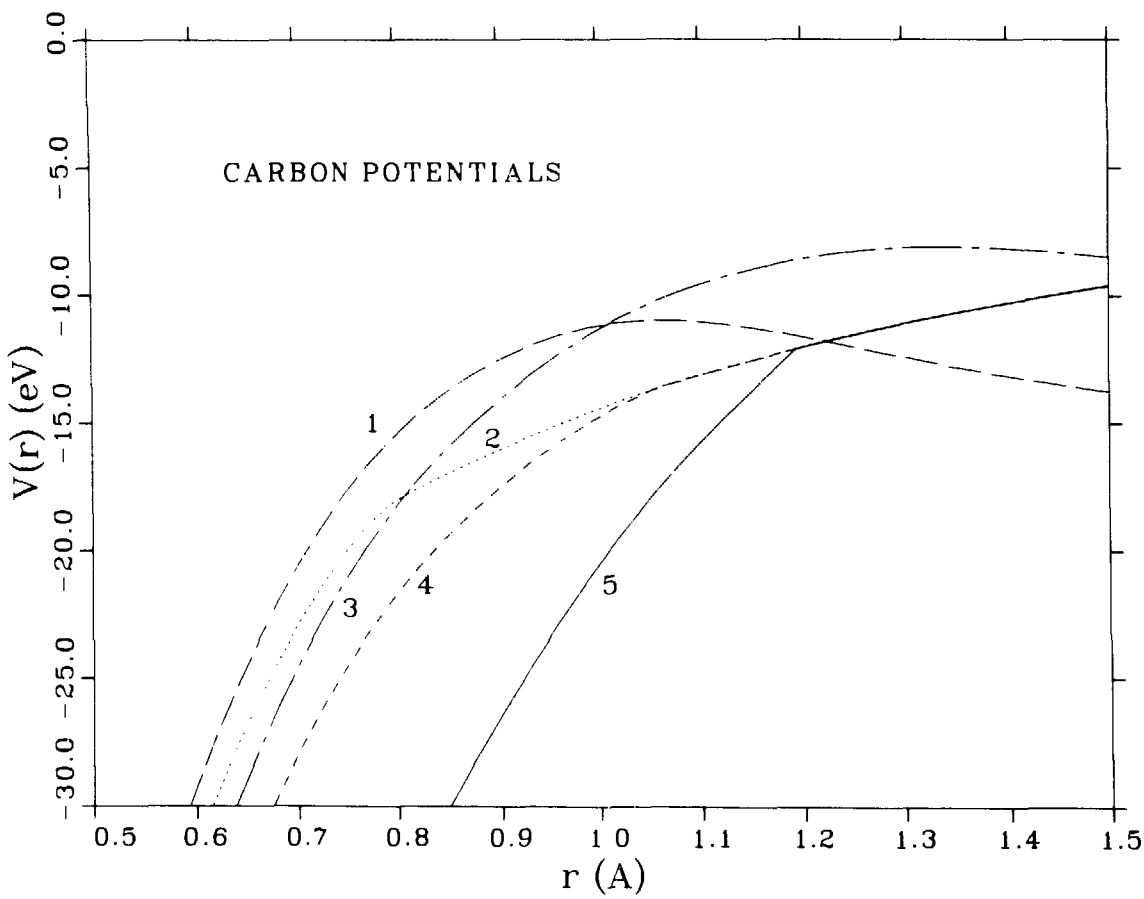

Fig. 1.
Electron-ion potentials near normal density and temperature. Numbers on the curves refer to definitions given in the text in Section 2.

2.1.2 $V_2(r)$

This is a modification of $V_1(r)$, which has an r^{-1} tail (a version of the Latter approximation) and is everywhere continuous and differentiable. It is defined by

$$V_2(r) = V_1(r) - V_1(r_0) - \alpha/r_0 \quad , \quad r \le r_0 \quad ,$$
$$= -\alpha/r \quad , \quad r \ge r_0 \quad , \tag{5}$$

where r_0 is defined by

$$\left.\frac{dV_1(r)}{dr}\right|_{r=r_0} = \frac{\alpha}{r_0^2} \quad . \tag{6}$$

2.1.3 $V_3(r)$

This is a TFD potential calculated for ρ=1.99526g/cm^3 and kT=10^{-2}eV. The corresponding value of r_t is 1.33630A.

2.1.4 $V_4(r)$

This is constructed from $V_3(r)$ in the same way that $V_2(r)$ is constructed from $V_1(r)$, through Eqs. (5) and (6).

2.1.5 $V_5(r)$

This is a self-consistent Dirac-Fock-Slater (DFS) potential calculated by the code HEX for the isolated-atom configuration $1s^2 3d^4$. This potential is defined as

$$V_s(r) = V_c(r) + V_x(r) - V_c(r_1) - V_x(r_1) - \alpha/r_1 \quad , \quad r \le r_1 \quad ,$$

$$= - \alpha/r \quad , \qquad\qquad r \ge r_1 \quad , \qquad (7)$$

where $V_c(r)$ and $V_x(r)$ are the usual Coulomb direct and Kohn-Sham exchange potentials for an atom with electron charge density $\rho_e(r)$, and r_1 is defined by

$$Z - 1 = \int_0^{r_1} d^3r \; \rho_e(r) \quad . \qquad (8)$$

The configuration $1s^2 3d^4$ was chosen in order to obtain a large band gap at diamond density $3.53 g/cm^3$. The calculated and experimental values are 4.67eV and 5.33eV, respectively. At graphite density $2.2 g/cm^3$, the band gap calculated from this potential is 8.6eV.

2.1.6 $V_{\rho T}(r)$

This is a linear combination of DFS and TFD potentials and is the actual potential used for each calculated temperature and density point. It is defined by

$$V_{\rho T}(r) = a\left[V_s(r) - V_s(r_t)\right] + (1-a)\left[V_t(r) - V_t(r_t)\right] \quad , \quad r \le r_t \quad ,$$

$$= 0 \quad , \qquad\qquad r \ge r_t \quad , \qquad (9)$$

where the mixing coefficient a is defined by

$$a = \frac{1}{(1 + \rho/\rho_0)(1 + T/T_0)} \quad , \qquad (10)$$

with $\rho_0 = 100 g/cm^3$ and $kT_0 = 100 eV$. $V_t(r)$ is a modified TFD potential similar to

$V_2(r)$ and $V_4(r)$, but it is calculated for the temperature and density of interest.

Potential regions are shown in Fig. 2. The regions in the ρ-T plane marked DFS and TFD are those for which the DFS or TFD potential mixing coefficients exceed 0.9. In the region marked MIX, both coefficients are less than 0.9.

2.2 Level structure

Piotted in Fig. 3 are the calculated eigenvalue magnitudes for the various densities between 10^{-3} and 10^{3}g/cm^3, for kT=10^{-2}eV, using the mixed potentials $V_{\rho T}(r)$. Solid lines represent bound states with E=-|E|, and dashed lines

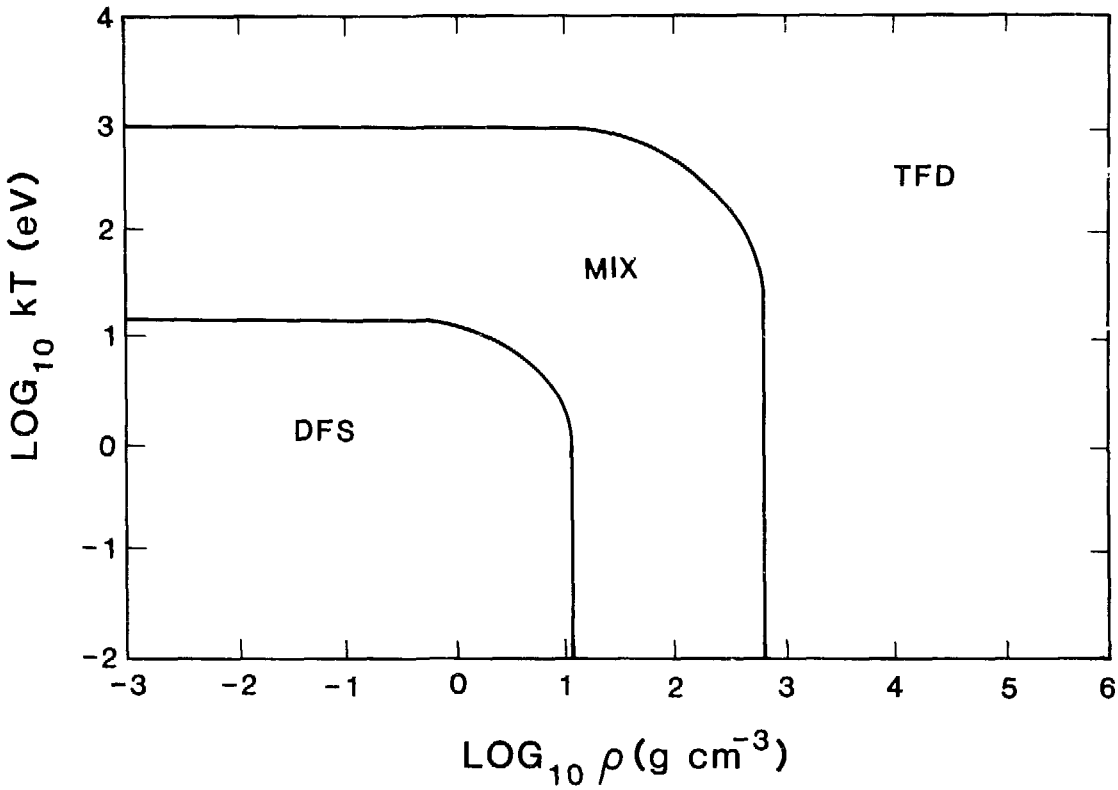

Fig. 2.
Potential regions in the ρ-T plane. The regions marked DFS and TFD are where these approximations account for at least 90% of the actual potential used. The region marked MIX is where neither approximation contributes as much as 90%.

represent continuum resonances with E=-|E|. The lines terminate for densities above which the corresponding resonance ceases to exist. The points marked with + represent bound-state energies at graphite and diamond densities.

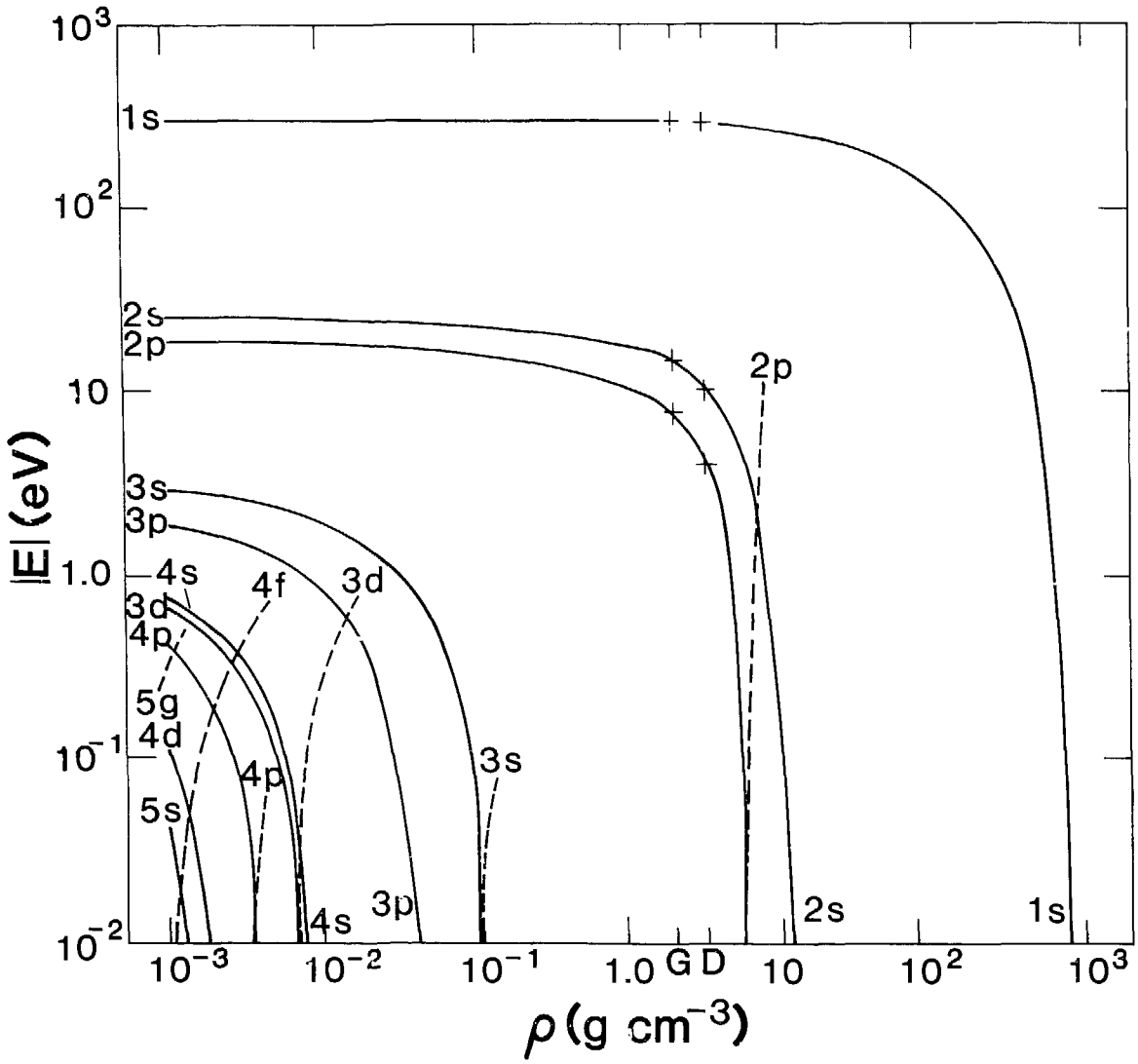

Fig. 3.
Electronic level structure for carbon at $kT=10^{-2}$eV, plotted as a function of density. Solid and dashed lines represent bound-state and continuum eigenvalue magnitudes, respectively. Densities marked G and D correspond to normal graphite and diamond densities, respectively.

2.3 Resonance softening

All resonances in the density of states and integrated cross section are broadened by direct convolution by means of

$$f(p) \rightarrow \frac{w}{\pi} \int_0^\infty dp' \; \frac{f(p')}{(p-p')^2 + w^2} \quad , \tag{11}$$

where f(p) is either dN/dp or

$$\Sigma(p) = \int_0^{2p} dq \; q^3 \; S(q) \; \sigma_\epsilon(q) \quad , \tag{12}$$

and $w^{-1}=20r_t$.

2.4 Angular momentum convergence

For each external momentum $p^2=(m+\epsilon)^2-m^2$, the maximum angular momentum for which partial waves are calculated is

$$|\kappa_x| = \mathrm{INT}\left[|\kappa_m| + 0.55pr_t + 2.5\right] \quad , \tag{13}$$

where κ_m is the highest channel for which a bound state or resonance has been found for that temperature and density. An overall limit $|\kappa_x| \leq 48$ is set; if κ_x exceeds this, the partial-wave calculation is abandoned. The region for which this occurs is marked "plane wave" in Fig. 4.

In the abandoned region, results are obtained using plane-wave calculations[5] as extrapolating functions. Define the new variables

$$x = Z_i/(Z-Z_i) \quad ,$$

$$y = \eta Z_i \quad , \tag{14}$$

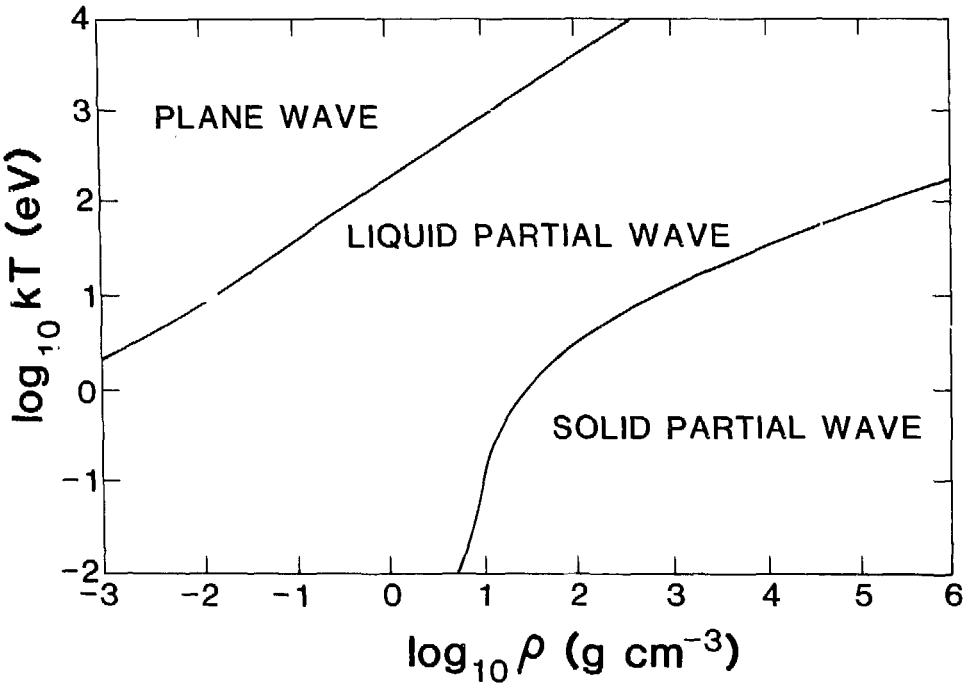

Fig. 4.
Calculational regions for carbon in the ρ-T plane. In the regions marked "partial wave," results are obtained by full partial-wave analysis. In the region marked "plane wave," results are obtained by combining partial-wave and plane-wave results. In the region marked "solid," the ion-ion coupling constant Γ exceeds 170, and the material is probably crystalline.

where Z_i and η are the ionization state and resistivity, respectively. These functions are defined so that x and y both lie between 0 and $+\infty$, and the leading dependence on Z_i is extracted from η. Multiplicative correction factors are obtained at the boundary where the partial-wave calculation fails by computing the ratios of the partial-wave to the plane-wave values of x and y. The correction factors are then extrapolated into the region where partial-wave results are not calculated with a stable averaging algorithm, in such a way that the boundary is crossed smoothly. If C_{jk} is an unknown correction factor, it is estimated by

$$C_{jk} = \frac{1}{2}\left[C_{j+1,k} + C_{j,k-1}\right] \quad , \tag{15}$$

where j and k stand for grid indices in the (ρ,T) plane. The grid is covered sequentially for decreasing ρ and increasing T, which insures that the correction factors on the right side of Eq. (15) are available when needed. These estimated factors are then used to correct the plane-wave results and reconstruct extrapolated values of Z_i and η.

2.5 Structure factors

For all ρ and T, the structure factor is interpolated from the one-component-plasma (OCP) structure factor calculated by Rogers et al.[6] These are plotted as a function of dimensionless momentum transfer qr_t and ion-ion coupling constant $\Gamma=Z_i^2\alpha\beta/r_t$ in Fig. 5.

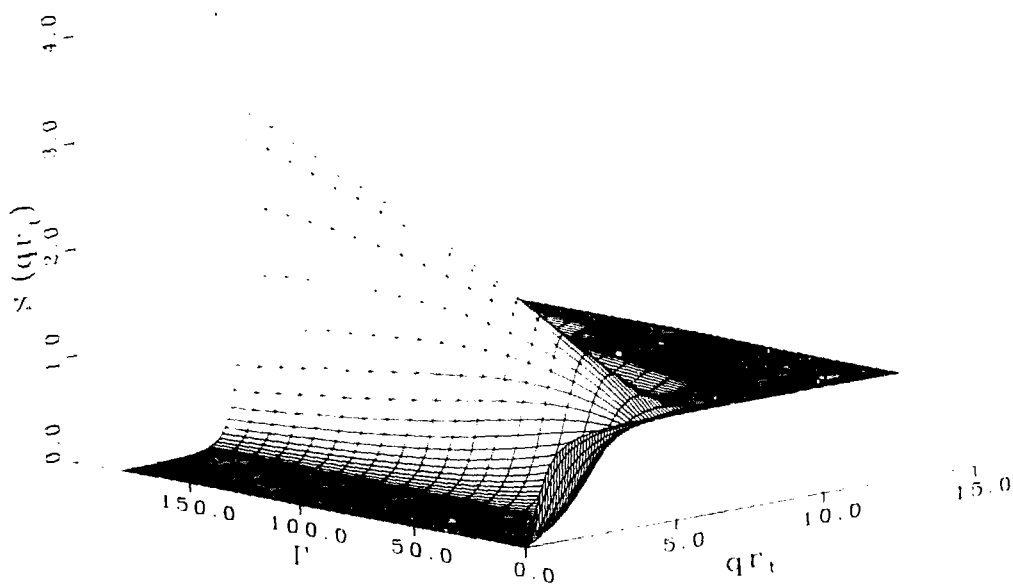

Fig. 5.
One-component-plasma structure factors, plotted as a function of dimensionless momentum transfer qr_t and ion-ion coupling constant Γ.

2.6 Thermal conduction

The thermal conductivity κ and thermoelectric coefficient S_{12} are calculated using a modification of the method of Lampe,[7,8] as described previously.[2-4] The only physical modification of Lampe's method is to replace his expression for the electron-ion Coulomb logarithm with a value that reproduces the present electrical conductivity $\sigma=\eta^{-1}$, thereby extending the validity of his results to more strongly coupled plasmas.

The coefficients are defined with respect to the transport equations

$$\underset{\sim}{J} = eS_{11}\left[e\underset{\sim}{E} + \frac{\Omega}{Z_i}\nabla P\right] + eS_{12}\frac{\nabla T}{T} \tag{16}$$

$$\underset{\sim}{Q} = -S_{12}\left[e\underset{\sim}{E} + \frac{\Omega}{Z_i}\nabla P\right] - S_{22}\frac{\nabla T}{T} + \frac{5}{3}\frac{\varepsilon}{e}\underset{\sim}{J} \quad , \tag{17}$$

where $\underset{\sim}{J}$ is the electric current, $\underset{\sim}{Q}$ is the heat flux, $\underset{\sim}{E}$ is the applied electric field, e is the electron charge, ε is the mean kinetic energy per electron, and $P=[(2/3)\varepsilon Z_i+kT]/\Omega$ is the pressure. The electrical conductivity σ and thermal conductivity κ (with the conventional constraint $\underset{\sim}{J}=0$) are

$$\sigma = e^2 S_{11} \tag{18}$$

$$\kappa = (S_{22} - S_{12}^2/S_{11})/T \quad . \tag{19}$$

S_{12} is the thermoelectric coefficient.

Some comments about units are in order. The quantity $[e\underset{\sim}{E}+\Omega\nabla P/Z_i]$ in Eqs. (16) and (17) has units energy$\cdot$length^{-1}. In order for the electron number current $\underset{\sim}{J}/e$ to have the proper units time^{-1}length^{-2}, S_{11} must have units energy^{-1}time^{-1}length^{-1}. If e^2 in Eq. (18) has the usual microscopic units energy$\cdot$length, i.e., $e^2\simeq 14.399758\text{eV}\cdot\text{A}\simeq 2.3071137\times10^{-19}\text{erg}\cdot\text{cm}$, then σ is in units time^{-1}. Units for σ in all tables and figures are sec^{-1}. Similarly, the last term in Eq. (16) requires S_{12} to have units length^{-1}time^{-1}. Tabulated values are cm^{-1}sec^{-1}.

The heat current Q has units energy•time^{-1}length^{-2}. This is consistent with the above units for S_{12}. It requires units energy•time^{-1}length^{-1} for S_{22}, which in turn requires units energy•deg^{-1}time^{-1}length^{-1} for κ. Tabulated values for κ are in units cm^{-1}sec^{-1}. This is appropriate if temperature is measured in energy units; otherwise, κ must be multiplied by the appropriate value of Boltzmann's constant k. The last term in Eq. (17) has the correct units in any consistent system.

3. Hydrogen calculations

In general, the calculations for hydrogen are carried out as for carbon, with the following modifications.

3.1 Electron-ion potentials

The mean-field approximations used for heavier ions are generally inappropriate for hydrogen. Application of the Latter approximation results in a potential that differs insignificantly from r^{-1}. Use of such a potential would effectively ignore the dielectric screening of the plasma. The importance of this error is not clear in the present context, where we are primarily interested in organic mixtures instead of pure hydrogen. Because we are not now prepared to address this question in detail, we have chosen simply to maintain consistency with the carbon calculation and set the electron-ion potential to $\alpha/r_t-\alpha/r$ for $r\le r_t$, and to 0 for $r>r_t$.

3.2 Level structure

Plotted in Fig. 6 are the calculated eigenvalue magnitudes for the various densities between 10^{-4} and 1 g/cm^3, for kT=10^{-2}eV, using the truncated r^{-1} potentials described above. Solid lines represent bound states with E=-|E|, and dashed lines represent continuum resonances with E=+|E|. The lines terminate for densities above which the corresponding resonance ceases to exist. The point marked with + represents the 1s bound-state energy at normal liquid density ρ=0.07g/cm^3.

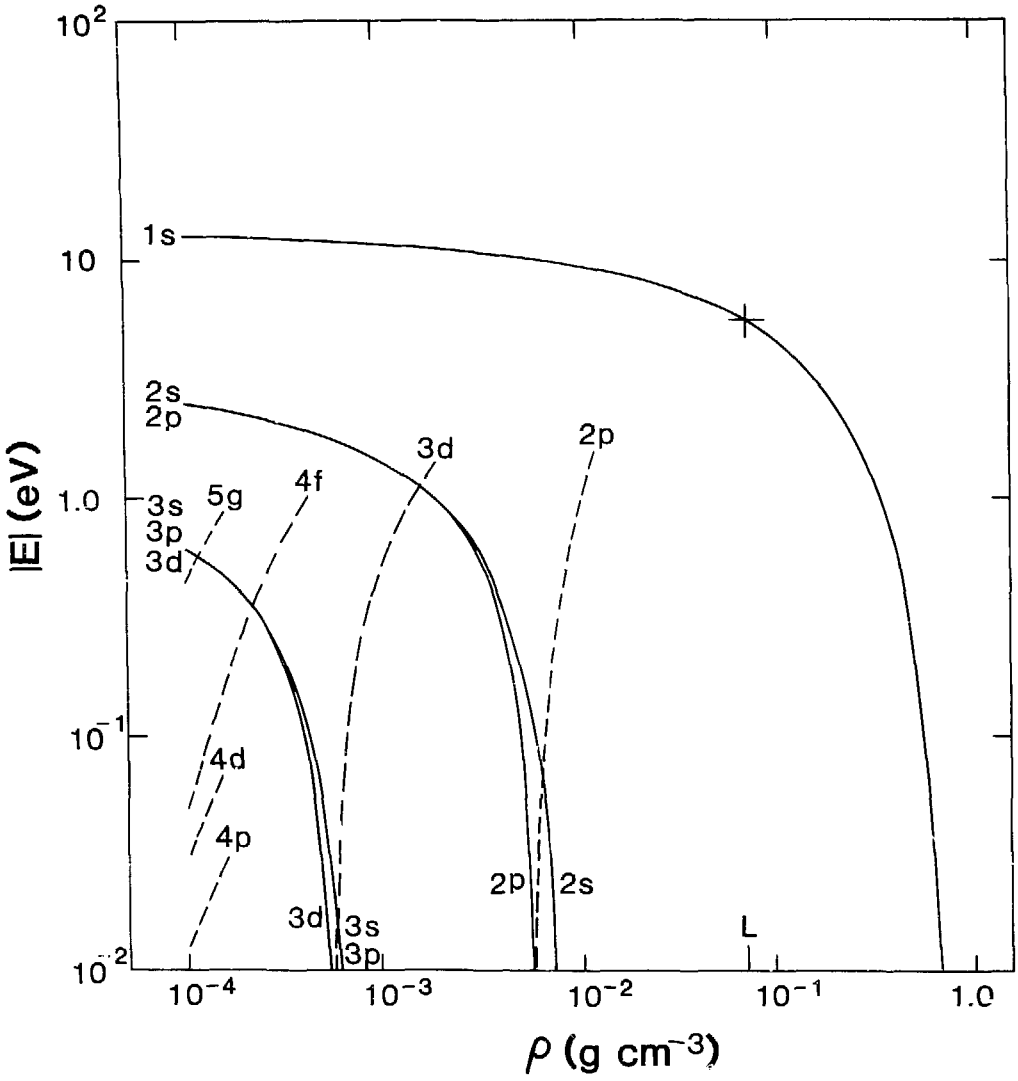

Fig. 6.
Electronic level structure for hydrogen at kT=10^{-2}eV, plotted as a function of density. Solid and dashed lines represent bound-state and continuum eigenvalue magnitudes, respectively. The density marked L corresponds to normal liquid density at 20K.

3.3 Angular momentum convergence

Some convergence difficulties were encountered near 10keV at the partial-wave boundary, making it necessary to modify Eq. (13) slightly in this region. The region for which the partial-wave calculation fails is marked "plane wave" in Fig. 7.

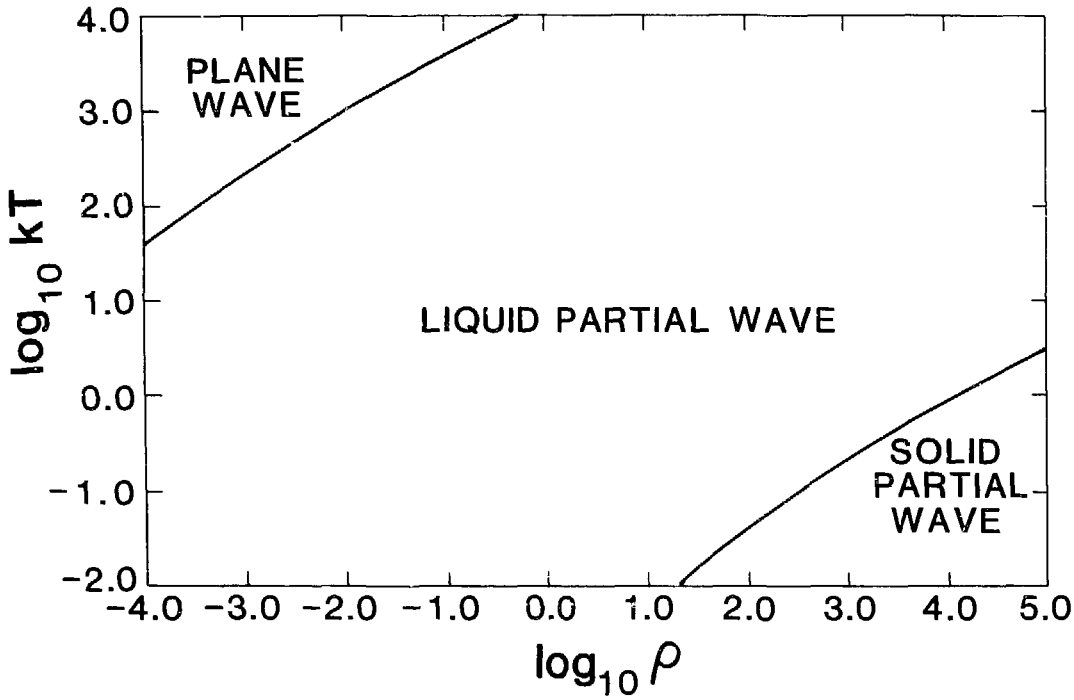

Fig. 7.
Calculational regions for hydrogen in the ρ-T plane. In the regions marked "partial wave," results are obtained by full partial-wave analysis. In the region marked "plane wave," results are obtained by combining partial-wave and plane-wave results. In the region marked "solid," the ion-ion coupling constant Γ exceeds 170, and the material is probably crystalline.

4. The organic mixture C_2H_3

We use a numerical mixing algorithm to combine the carbon and hydrogen results for the atomic ratio C_2H_3. For a given temperature, the carbon and hydrogen tables are searched for the partial densities that yield the same ionization state per unit volume and reproduce the correct overall mixture density. This procedure is equivalent to requiring the chemical potential to be

constant throughout the volume of the mixture. The ionization state per ion in the mixture is the weighted average of the two species, with respective weights two and three. The electrical conductivities are combined following the method of Landauer,[9] in which the same weighted average of the logarithms is taken. The thermal transport coefficients are computed from the combined ionization states and conductivities by the methods described in Sec. 2.6.

5. Results

Tabulated values of Z_i, σ, κ, S_{12}, and the conductive opacity

$$\kappa_e = \frac{16}{3} \frac{\sigma_{sb}}{k} \frac{T^3}{\rho\kappa} \quad , \tag{20}$$

where $\sigma_{sb}/k=4.10696\times10^{11}s^{-1}cm^{-2}K^{-3}$, are available in the Los Alamos SESAME Library. Units for κ_e are cm^2/g. These functions, as well as some related plasma parameters and comparisons to other work, are also available from the author. Plasma parameters that have not been defined so far in the text are the plasma frequency

$$\frac{\hbar\omega_p}{kT} = \left[\frac{3\,\Gamma}{kTMr_t^2}\right]^{1/2} \quad , \tag{21}$$

where M is the ion mass; the Debye radius

$$\frac{r_d}{r_t} = (3\Gamma)^{-1/2} \quad , \tag{22}$$

and the classical mean free path

$$\lambda = \frac{\sigma\Omega}{Z_i\alpha} \langle p^2 \rangle^{1/2} \quad , \tag{23}$$

where we define the average momentum

$$\langle p^2 \rangle \cdot \int_0^\infty dp\ p^2\ f'(\epsilon) = \int_0^\infty p^4\ f'(\epsilon) \quad . \tag{24}$$

This average selects those momenta near the Fermi momentum for the degenerate case and approaches the ideal gas limit for large kT.

Three results of different models to which comparisons are made are σ_{HL}, the electrical conductivity as calculated by the complete method of Hubbard and Lampe;[8] $\kappa_{LG}=4kT\sigma/\alpha$, the thermal conductivity as calculated in the degenerate Lorentz gas model; and $S_{LG}=3\kappa_{LG}/8$, the degenerate Lorentz gas thermoelectric coefficient. Note that these last two quantities differ in definition from those adopted here by the convective current term in Eq. (17).

The principal results of the present calculation are displayed in Figs. 8-19. All functions are plotted versus ρ in g/cm^3 and kT in eV. Figures 8-10 show ionization states for the two elements and for the mixture. The insulating region at low temperature and density is clearly evident in all three cases. The gas-plasma transition, which is due to thermal ionization as kT increases, and the insulator-metal transition, which is due to pressure ionization as ρ increases, are qualitatively similar for each material. The most interesting detail is the sharp metal-insulator transition in hydrogen at high density and low temperature. This corresponds to pressure ionization of the 1s state. The effect is large for three reasons: 1) when it enters the continuum, the 1s state immediately spreads out over a range of energies, failing to persist as a resonance because there is no angular momentum barrier to confine it; 2) the potential is not self-consistent, so that it cannot adjust to compensate partially for the striking change in the electron wave function; and 3) there are no other electrons present to reduce the relative importance of the effect. This effect persists in reduced magnitude for the mixture. The boundary between the partial-wave calculation and the renormalized plane-wave approximation is invisible. Figures 11-19 show the electrical and thermal

conductivities and thermoelectric coefficient. The same qualitative remarks apply.

Figures 20-22 show the ion-ion coupling constant Γ. Where this is greater than 170 ($\log_{10}\Gamma \simeq 2.23$), one can expect the plasma to have crystallized, so that the present amorphous approximations become inappropriate and the results increasingly inaccurate as Γ increases beyond this. Also plotted is the boundary μ=kT separating the degenerate region μ>kT from the nondegenerate region μ<kT. Figures 23-25 show the electron mean free path λ in units r_t. Where this is less than $\simeq$1, ($\log_{10}\lambda/r_t \simeq 0$), the material is effectively an insulator, and this parameter loses its physical meaning.

Figures 26-31 show comparisons to other approximate models. Figures 26-28 show the ratio of the present electrical conductivities to those calculated by the method of Hubbard and Lampe, given the ionization states displayed in Figs. 8-10. Discrepancies of both signs appear. The floor in each figure represents the region in which Hubbard and Lampe consider their calculation to be invalid. Figures 29-31 show the ratio of thermal conductivity to that calculated in the Lorentz gas model, given the ionization states and electrical conductivities displayed in Figs. 8-13. As originally noted by Lampe,[7] discrepancies are most important for low density near the gas-plasma transition, at the onset of thermal ionization. This arises from the importance of electron-electron collisions. At relatively low temperatures, the electrons are not particularly energetic and the ions not highly charged, so that collisions with other electrons are important. As kT increases for pure carbon, collisions with the more highly charged ions begin to dominate, the electron-electron collisions become relatively less important, and the thermal conductivity approaches the Lorentz gas limit. For hydrogen, the electron-ion collisions never dominate outside the degenerate region because the ions cannot acquire a charge greater than one. The organic mixture exhibits a partial return to the Lorentz gas at high temperature and low density. The contour plots of Figs. 29-31 also display solid lines for the contour $\sigma=\sigma_{HL}$, and dashed lines for the contour $\sigma=0.3\sigma_{HL}$.

6. Comparison with experiment

Meaningful comparison with experiment is complicated by a lack of data in the liquid and plasma regimes, where the present model is applicable. Measurements are available for carbon only in its nonmetallic or semimetallic crystalline phases near normal temperature and density. Here, all transport properties are sensitive functions of the lattice structure. Diamond is an electrical insulator with thermal conduction due entirely to lattice vibrations. Graphite is an anisotropic electrical conductor, with thermal conduction due both to electron transport and lattice phonons. The present model predicts no electrical conduction at either diamond or graphite density. It also predicts no thermal conduction, because here this depends entirely upon electron transport. It is not possible to determine at present whether any meaning can be attached to the results for the metallic solid region, where nearly free electrons may dominate the transport properties.

The most interesting point of comparison for hydrogen is the density of the metal-insulator transition. Our results suggest that this should occur at $\rho \approx 0.7 g/cm^3$. This is close to but slightly less than the $1 g/cm^3$ reported in a magnetic implosion experiment.[10]

The thermal and electrical properties of organic compounds have been studied extensively near normal conditions but not in the regions of significant ionization, where the effects of molecular structure become unimportant.

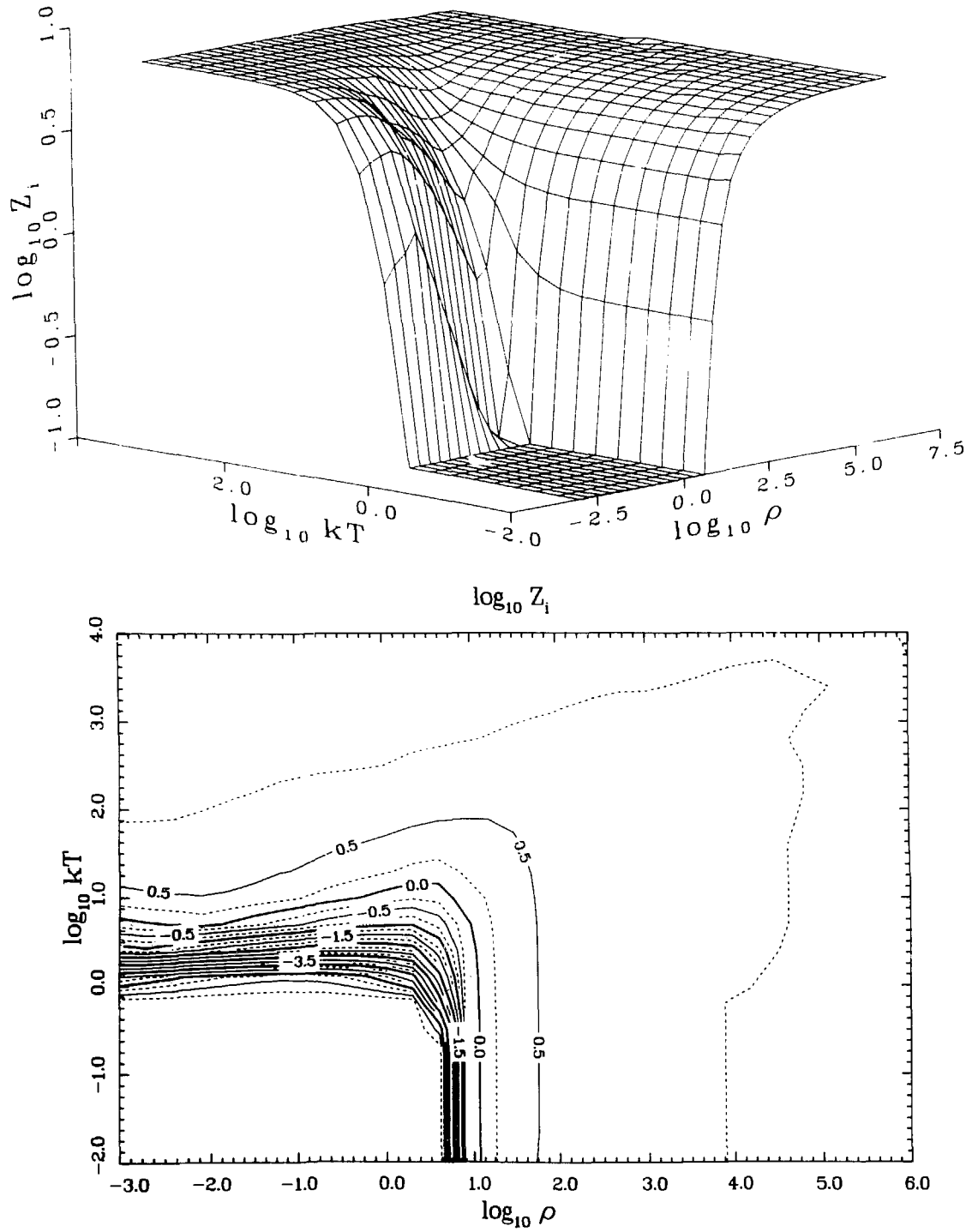

Fig. 8.
Ionization state Z_i for carbon as a function of temperature and density.

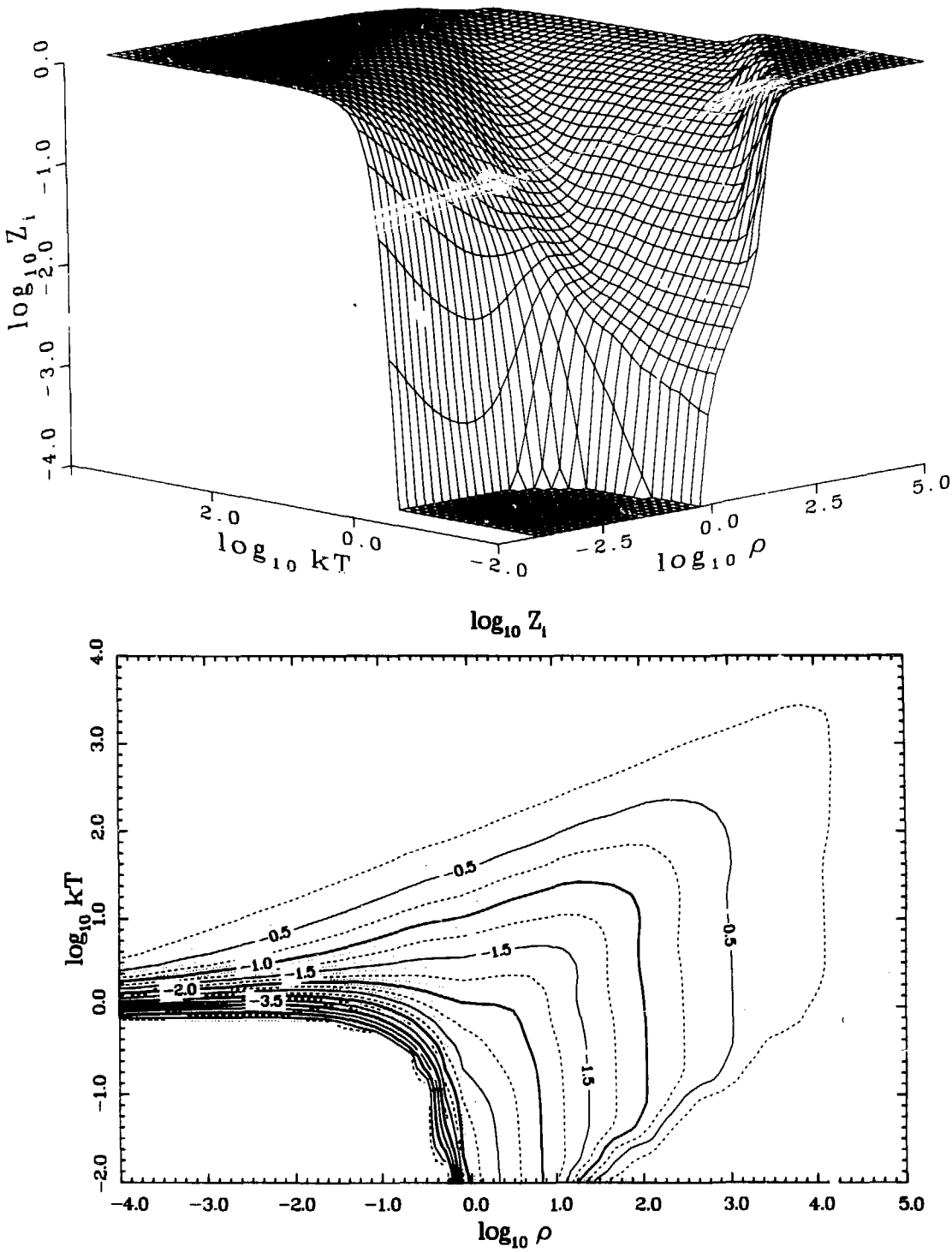

Fig. 9.
Ionization state Z_i for hydrogen as a function of temperature and density.

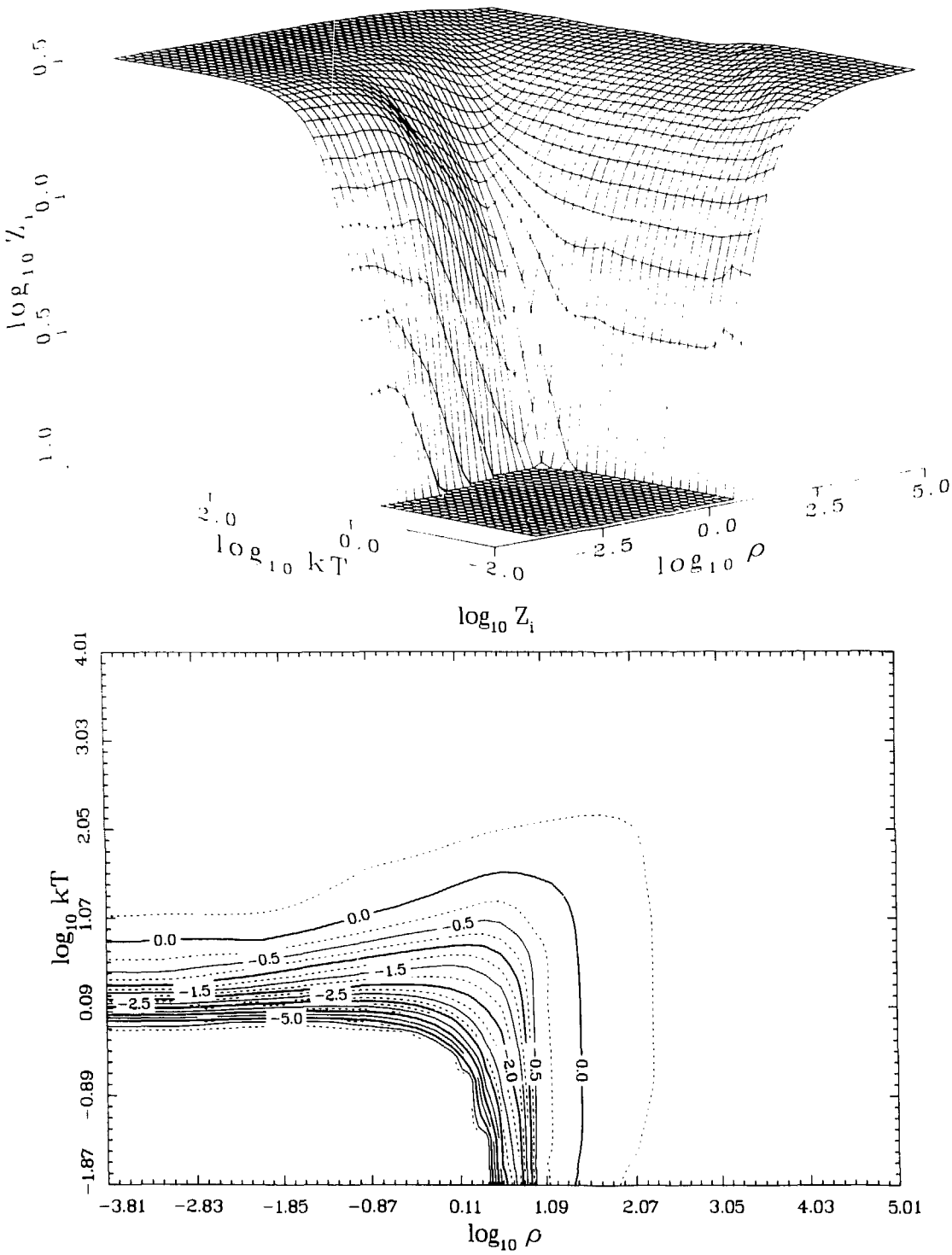

Fig. 10.
Ionization state Z_i for C_2H_3 as a function of temperature and density.

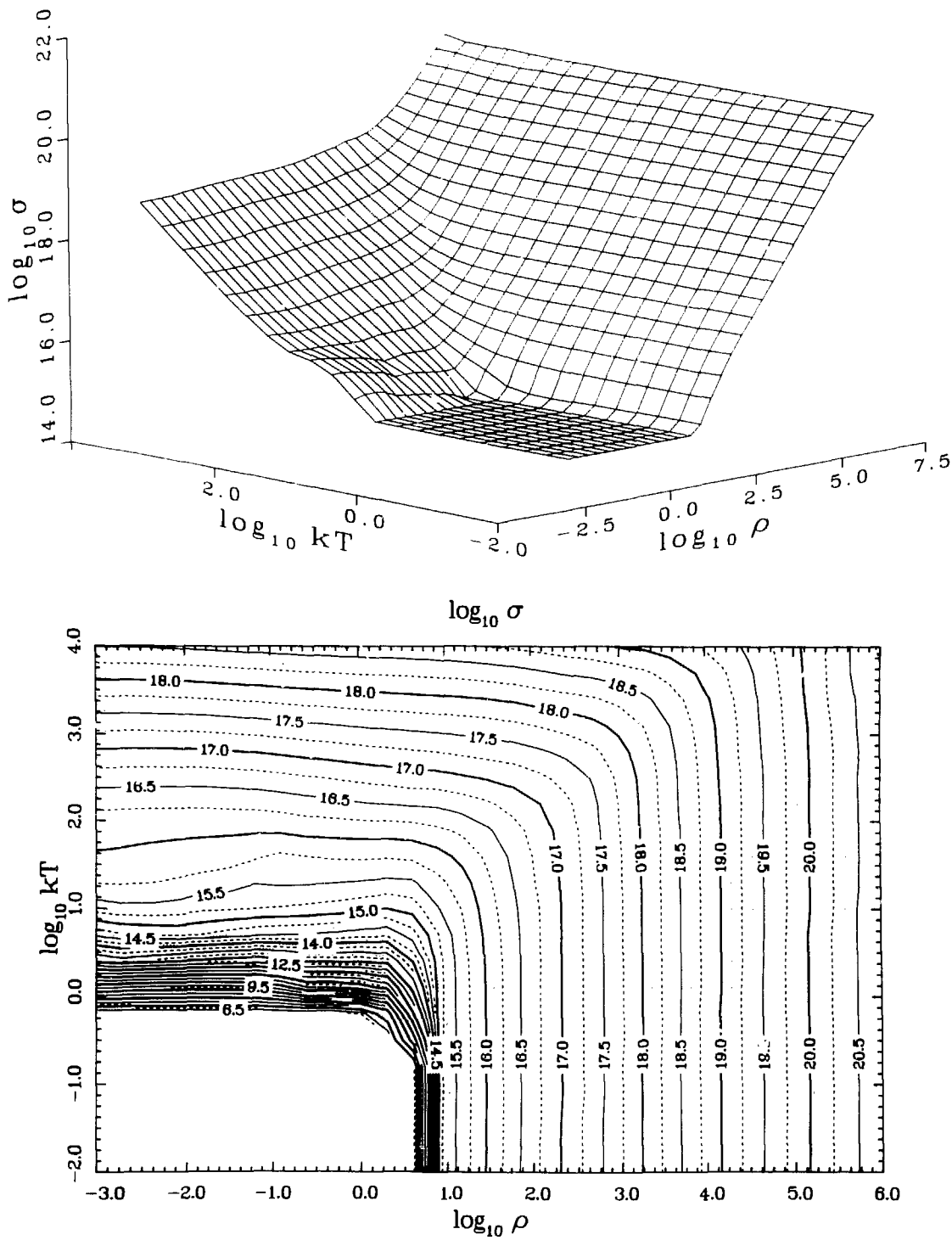

Fig. 11.
Electrical conductivity σ (s^{-1}) for carbon as a function of temperature and density.

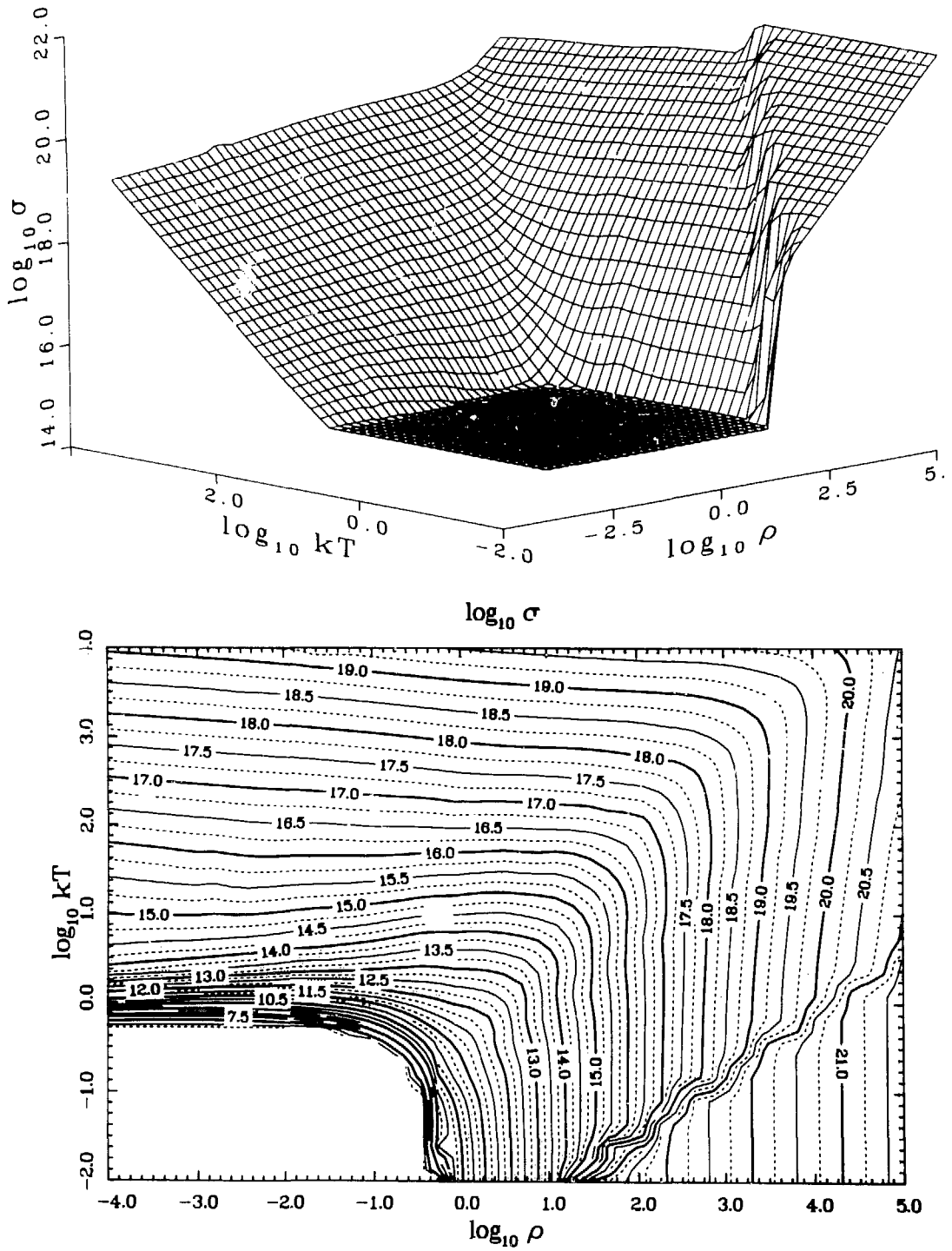

Fig. 12.
Electrical conductivity σ (s^{-1}) for hydrogen as a function of temperature and density.

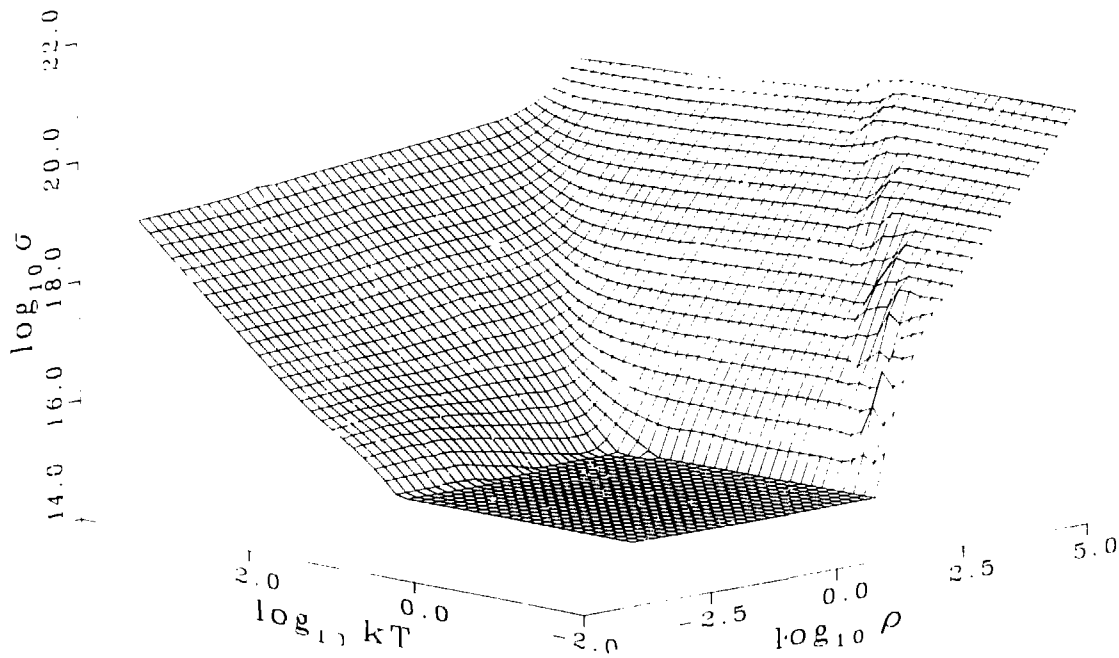

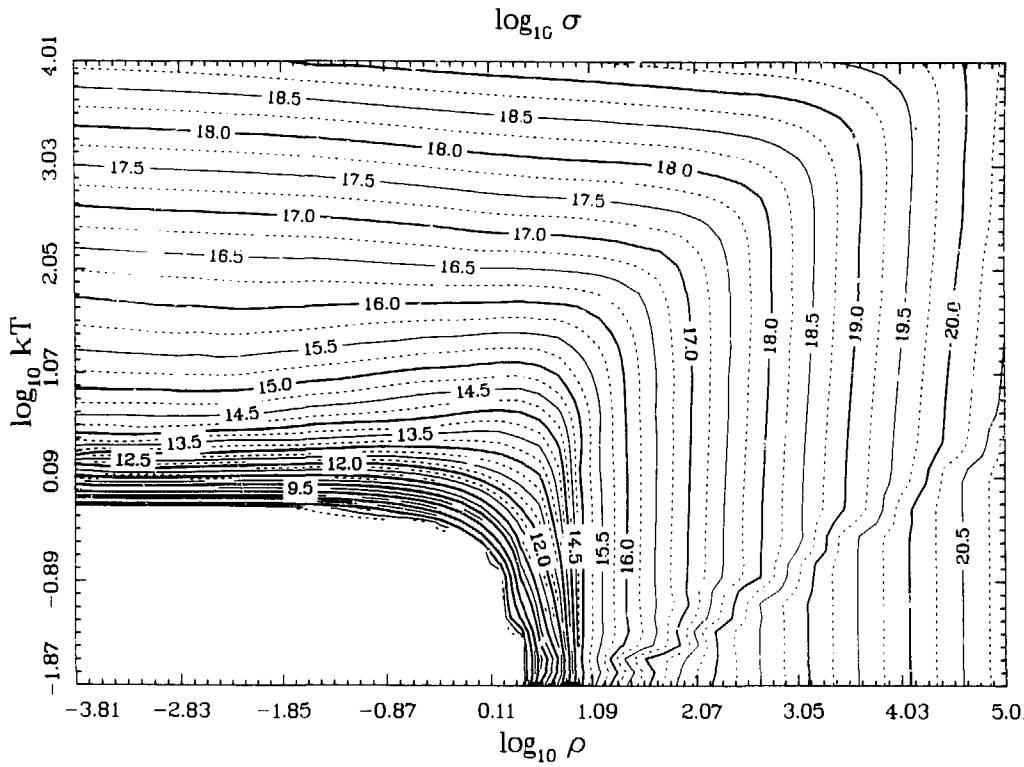

Fig. 13.
Electrical conductivity σ (s^{-1}) for C_2H_3 as a function of temperature and density.

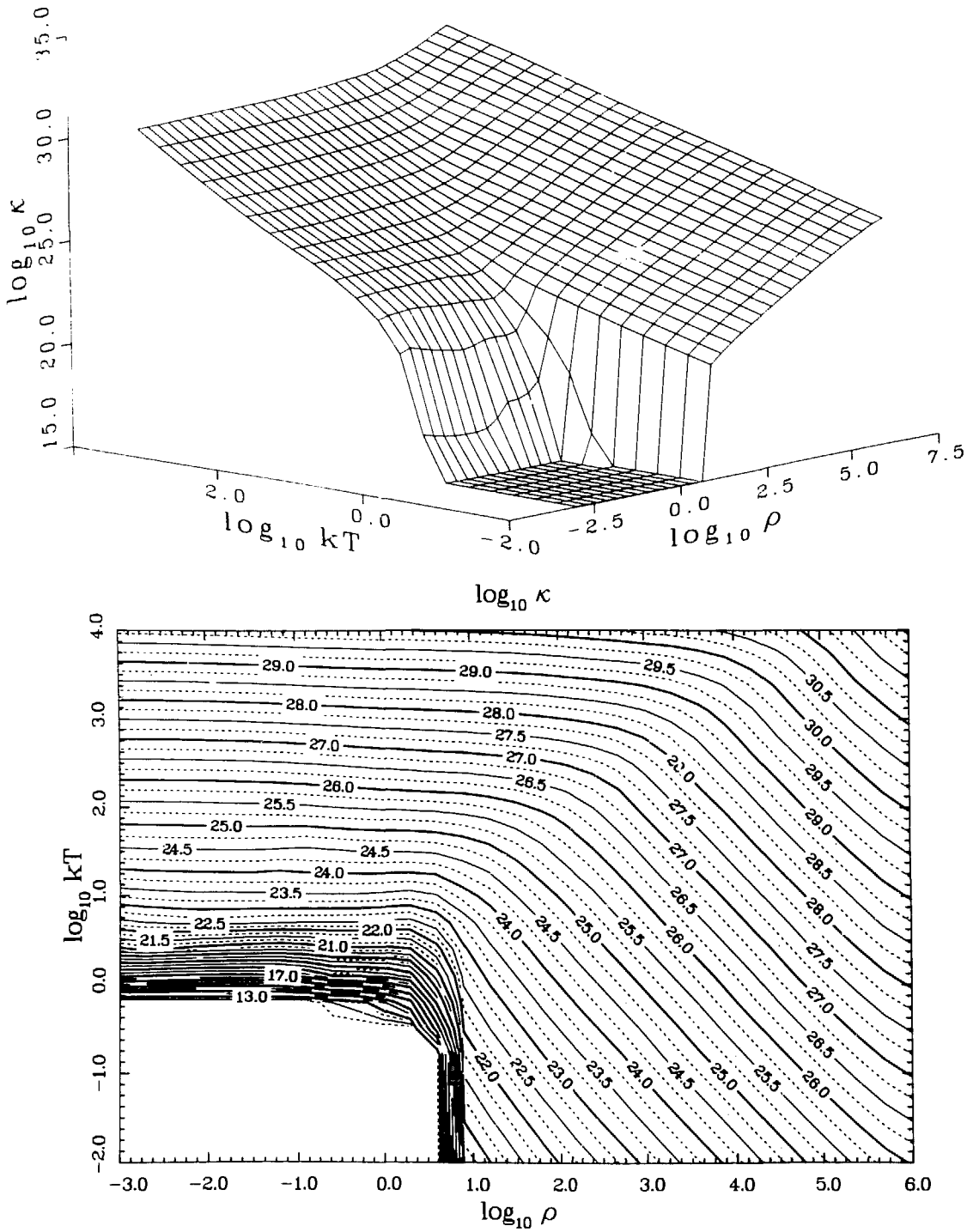

Fig. 14.
Thermal conductivity κ ($cm^{-1}s^{-1}$) for carbon as a function of temperature and density.

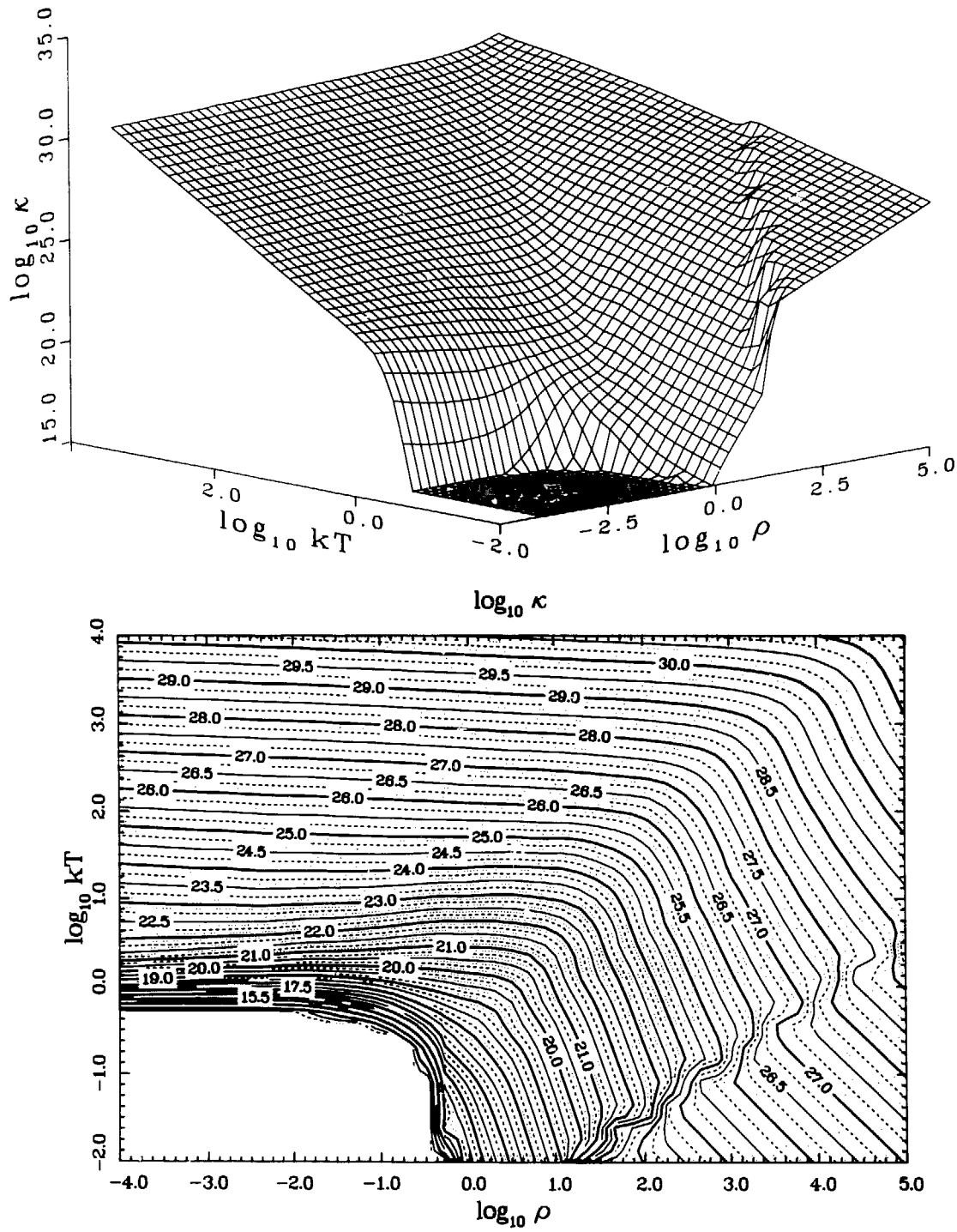

Fig. 15.
Thermal conductivity κ ($cm^{-1}s^{-1}$) for hydrogen as a function of temperature and density.

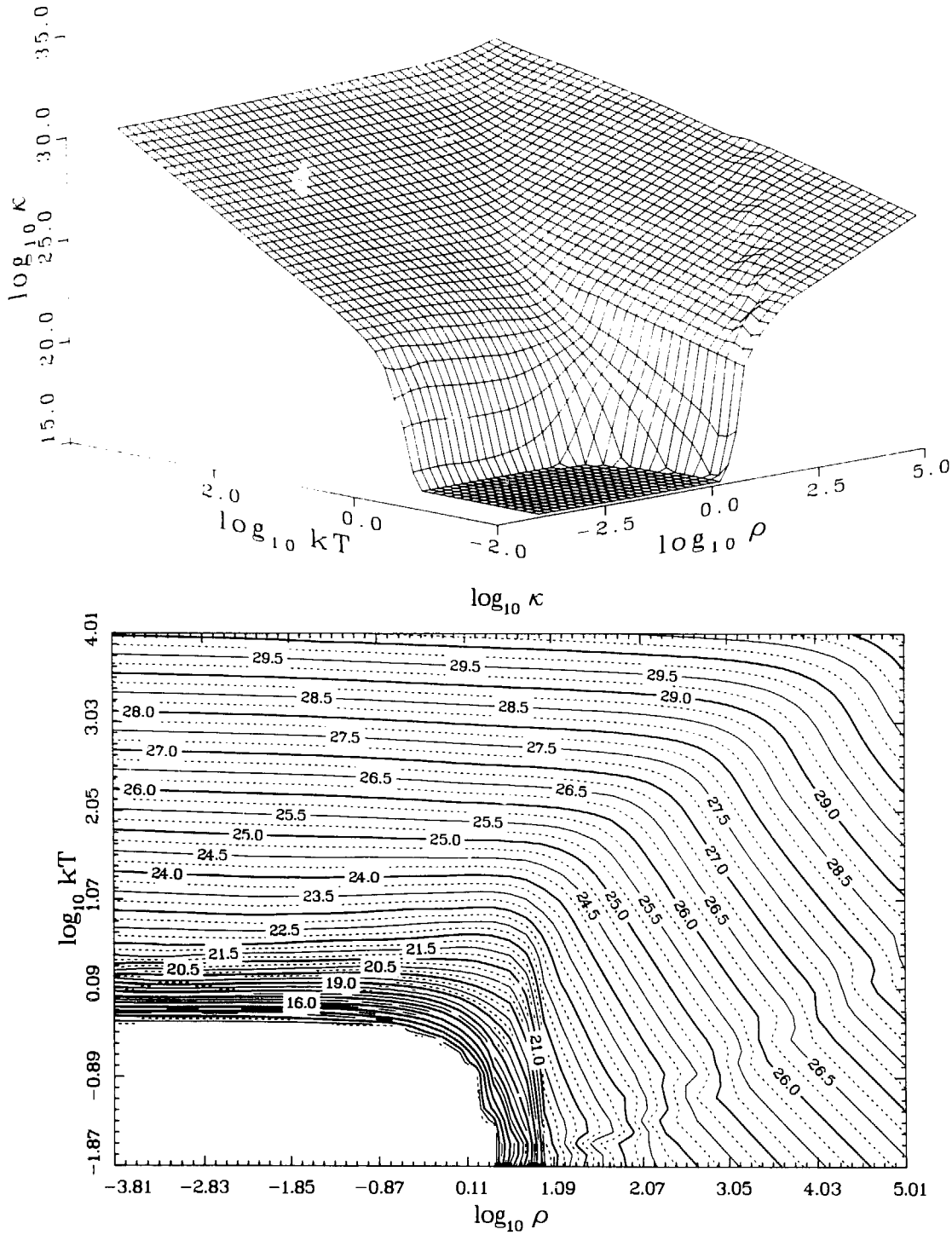

Fig. 16.
Thermal conductivity κ ($cm^{-1}s^{-1}$) for C_2H_3 as a function of temperature and density.

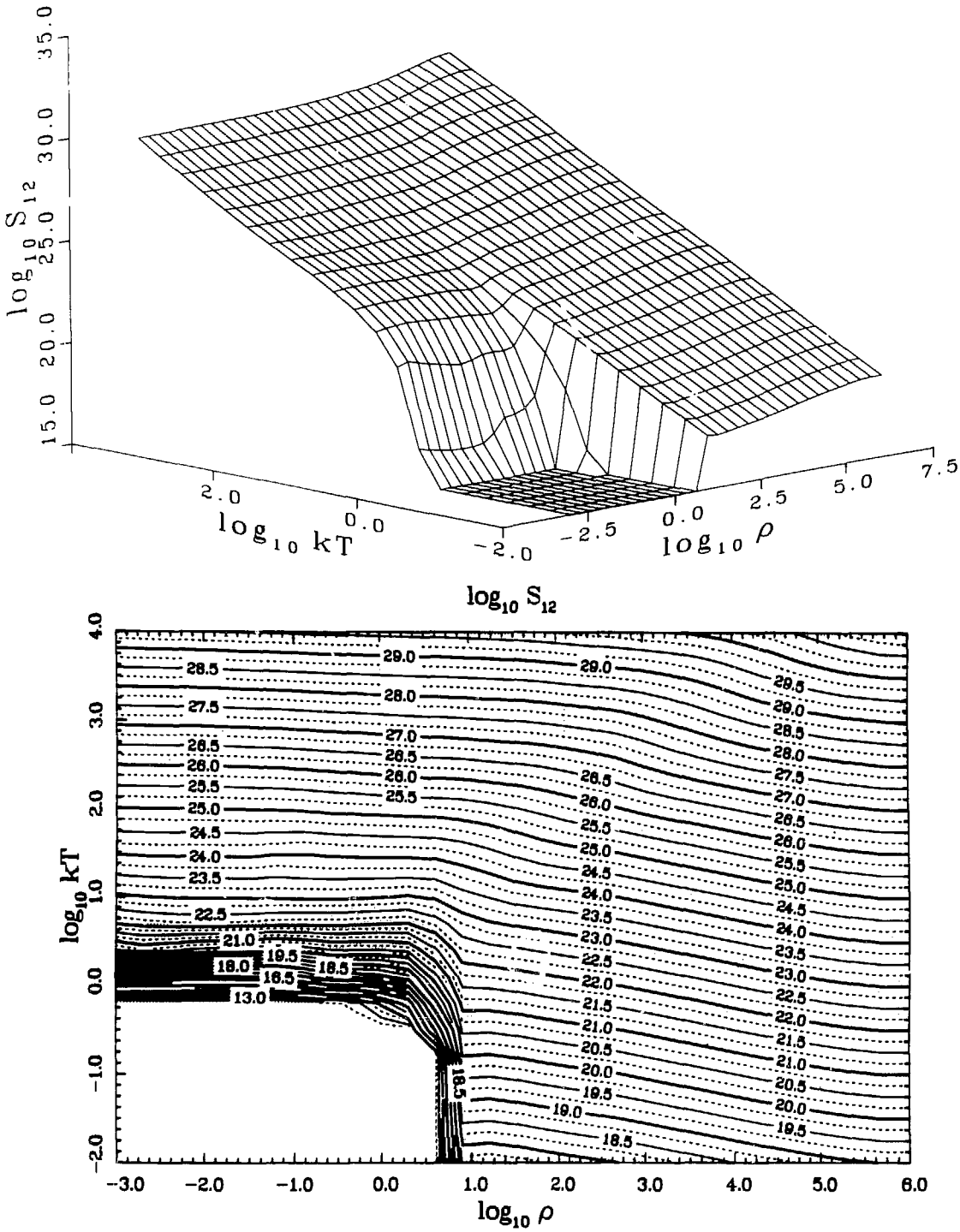

Fig. 17.
Thermoelectric coefficient S_{12} ($cm^{-1}s^{-1}$) for carbon as a function of temperature and density.

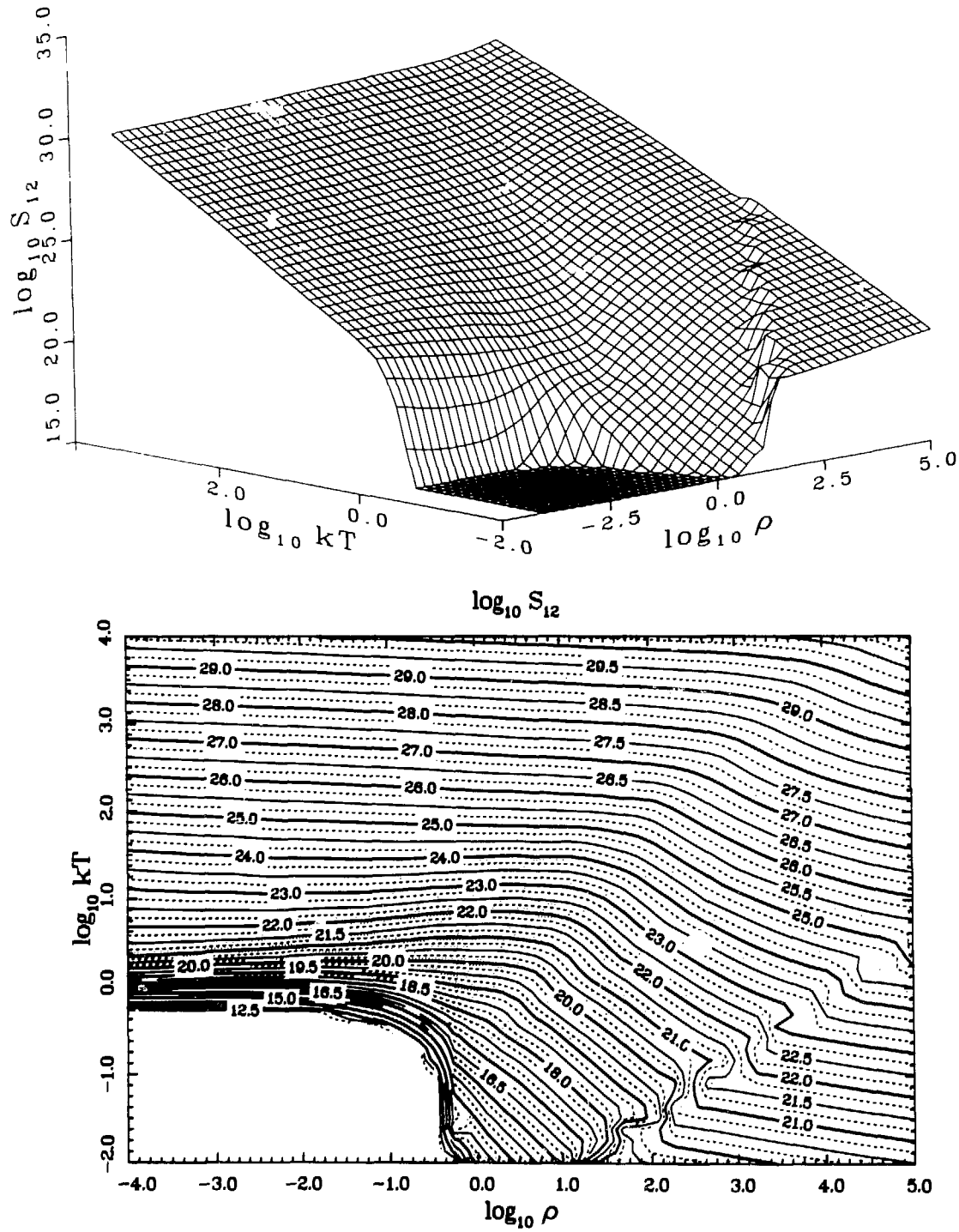

Fig. 18.
Thermoelectric coefficient S_{12} ($cm^{-1}s^{-1}$) for hydrogen as a function of temperature and density.

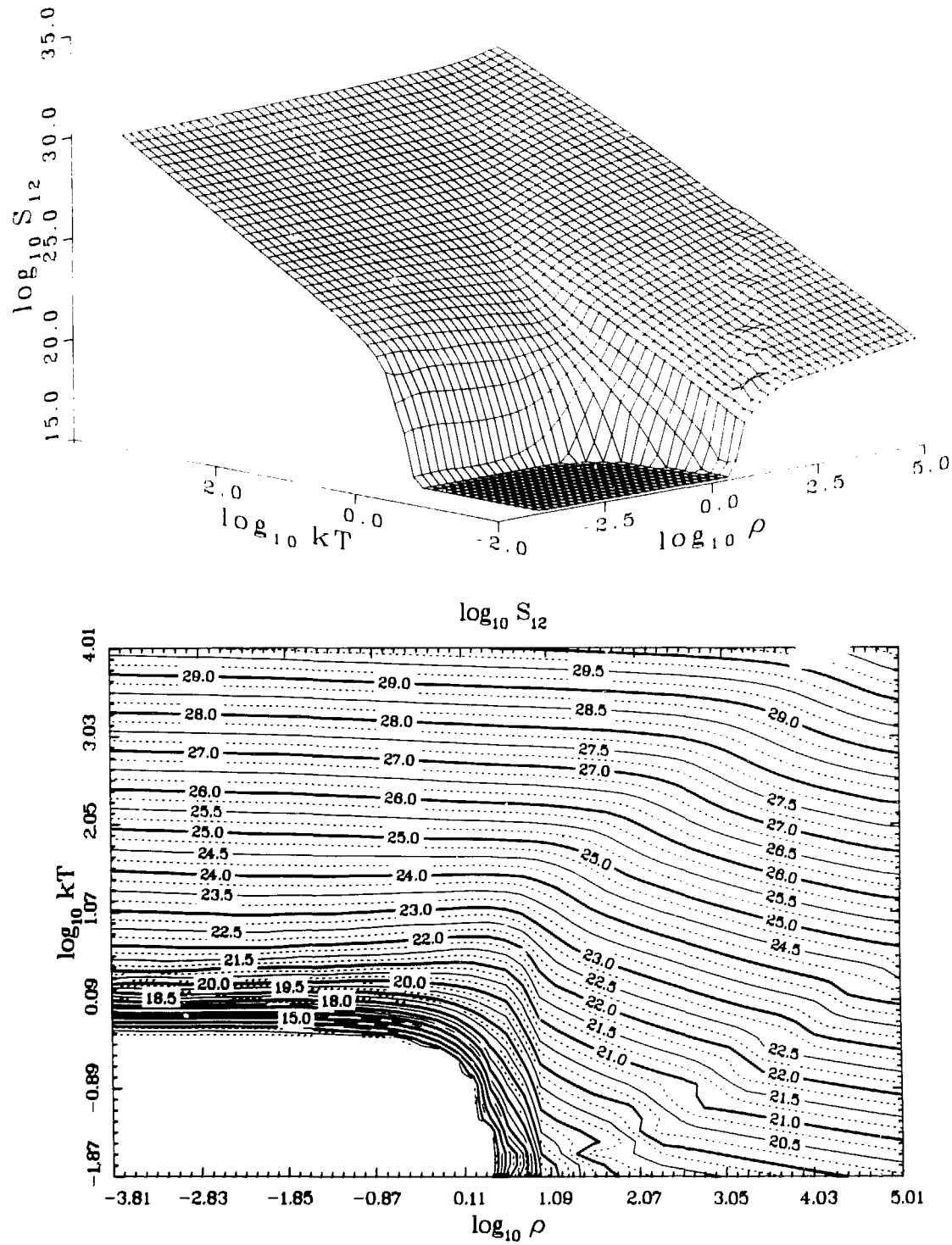

Fig. 19.
Thermoelectric coefficient S_{12} ($cm^{-1}s^{-1}$) for C_2H_3 as a function of temperature and density.

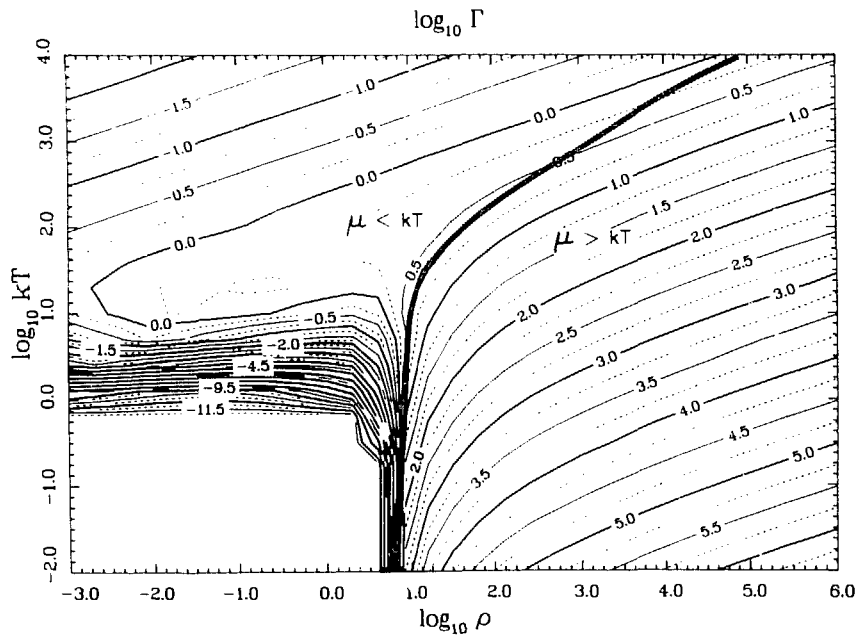

Fig. 20.
Ion-ion coupling constant Γ for carbon as a function of temperature and density. The heavy solid line delineates the degenerate region (μ>kT) from the nondegenerate region (μ<kT).

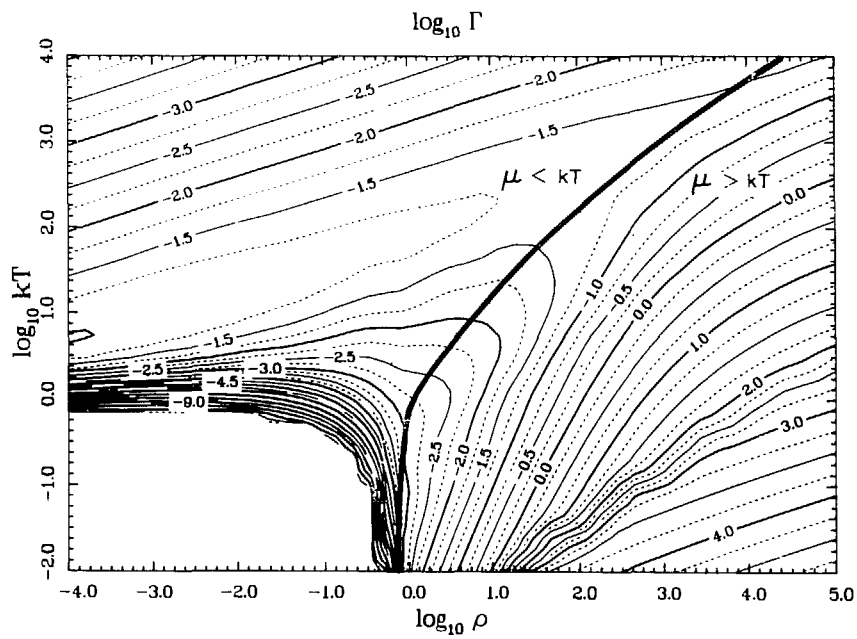

Fig. 21.
Ion-ion coupling constant Γ for hydrogen as a function of temperature and density. The heavy solid line delineates the degenerate region (μ>kT) from the nondegenerate region (μ<kT).

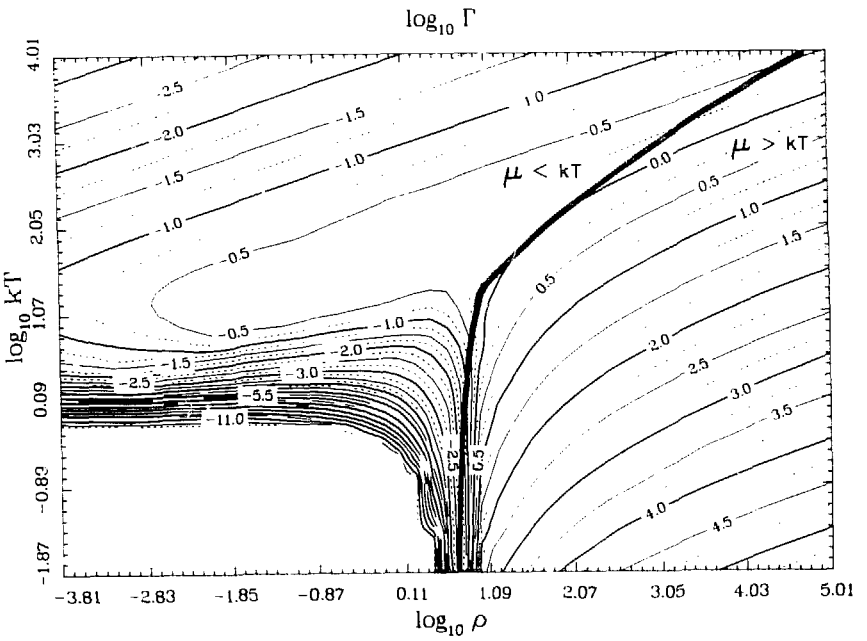

Fig. 22.
Ion-ion coupling constant Γ for C_2H_3 as a function of temperature and density. The heavy solid line delineates the degenerate region (μ>kT) from the nondegenerate region (μ<kT).

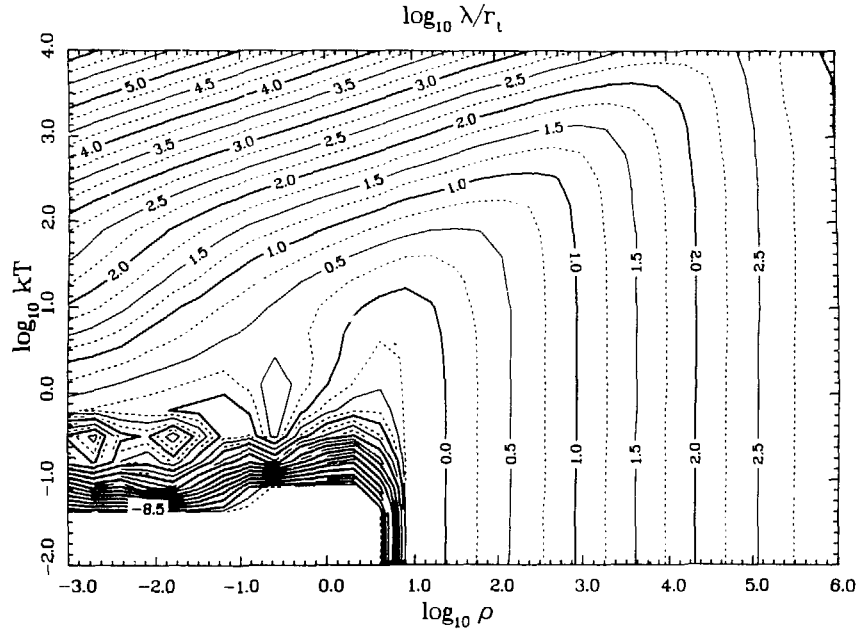

Fig. 23.
Electron mean free path λ/r_t for carbon as a function of temperature and density.

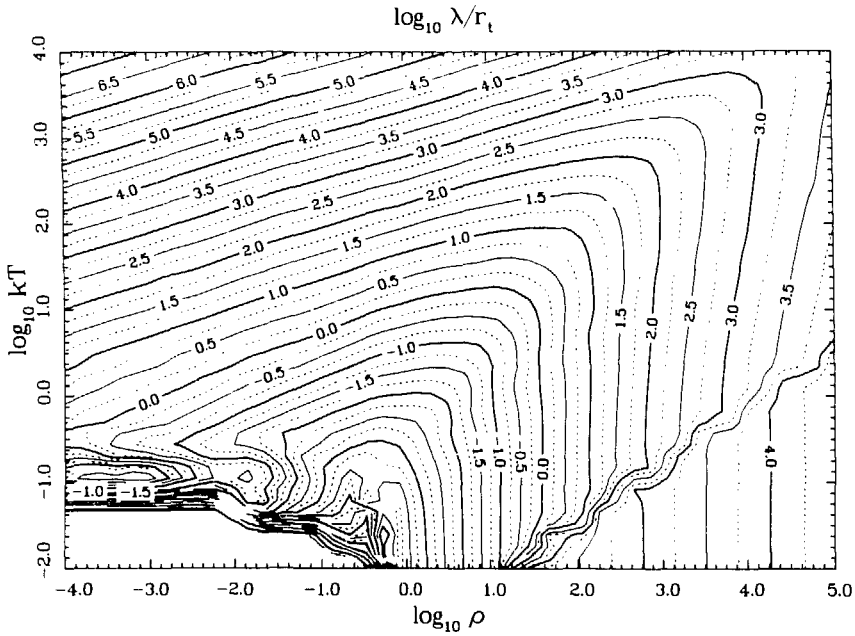

Fig. 24.
Electron mean free path λ/r_t for hydrogen as a function of temperature and density.

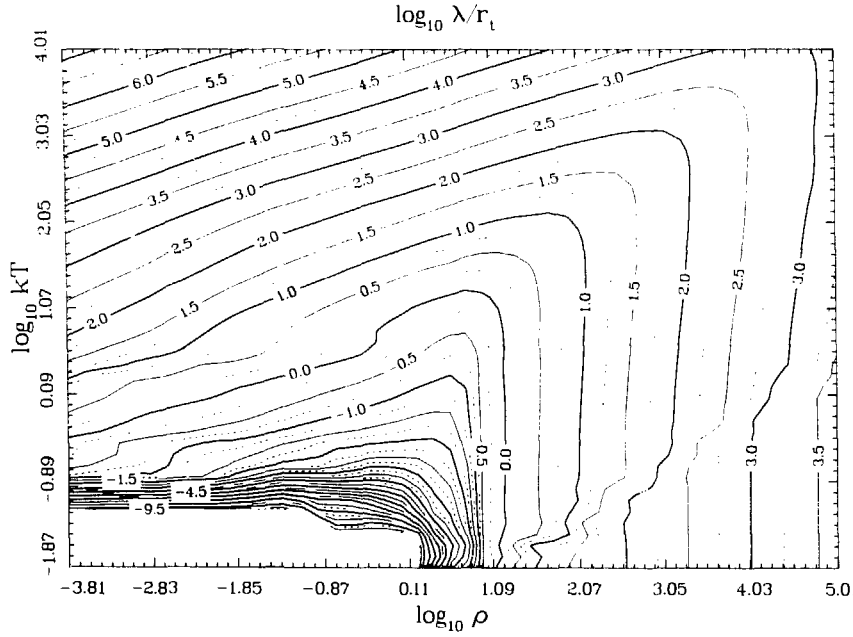

Fig. 25.
Electron mean free path λ/r_t for C_2H_3 as a function of temperature and density.

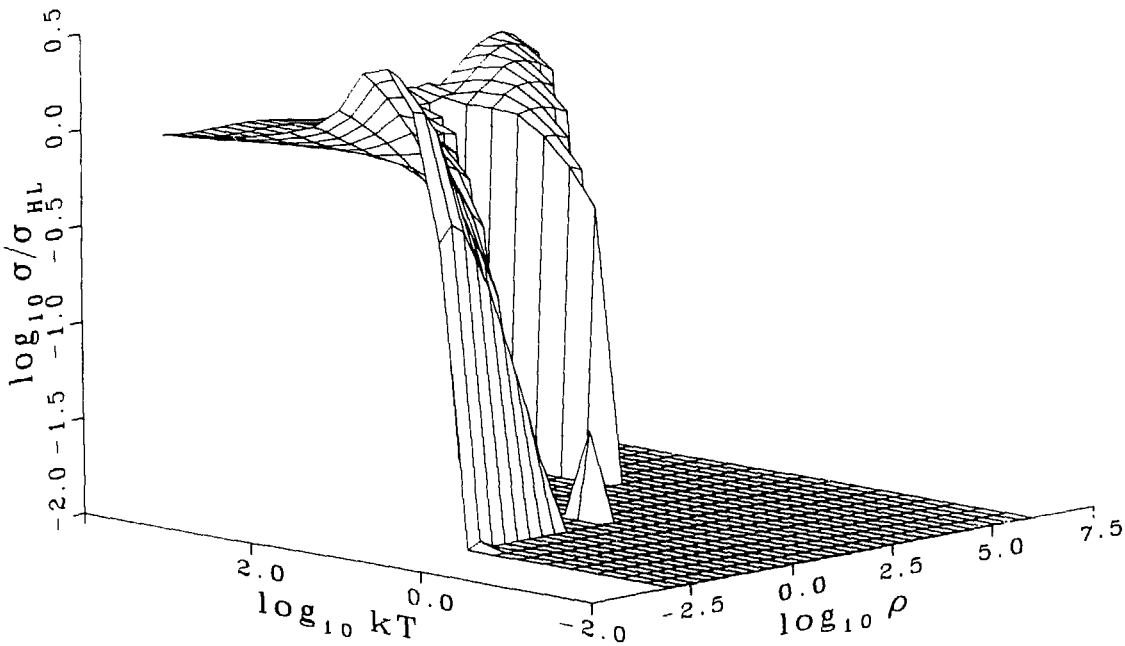

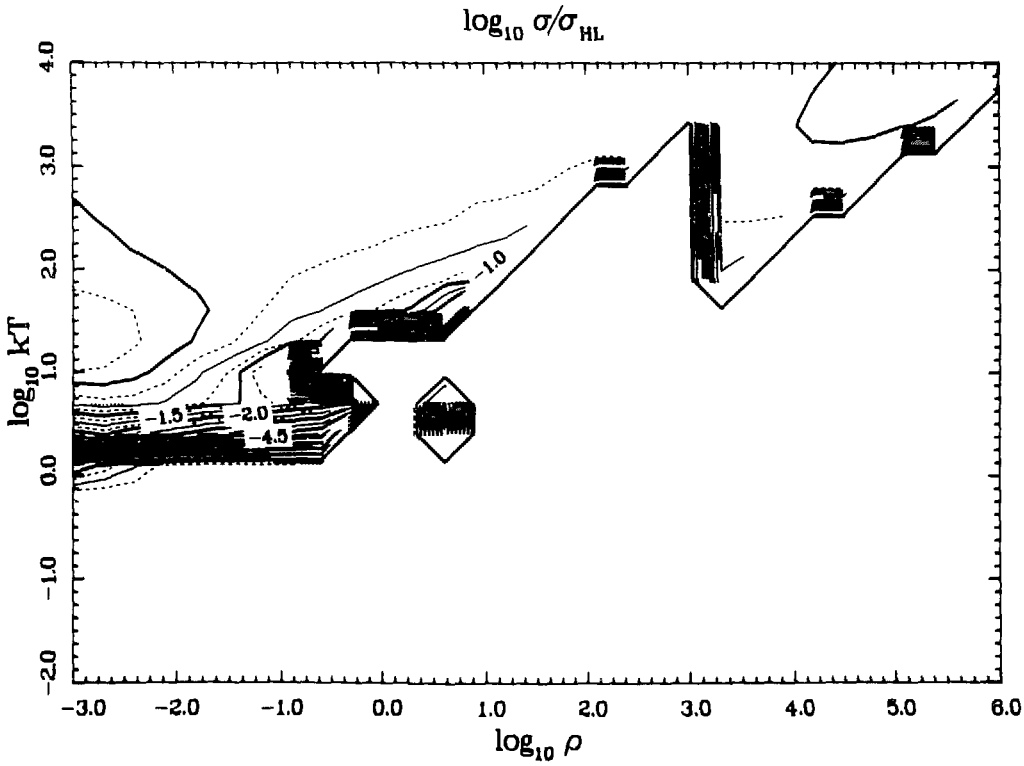

Fig. 26.
Comparison of calculated electrical conductivity σ with the method of Hubbard and Lampe σ_{HL}, for carbon as a function of temperature and density.

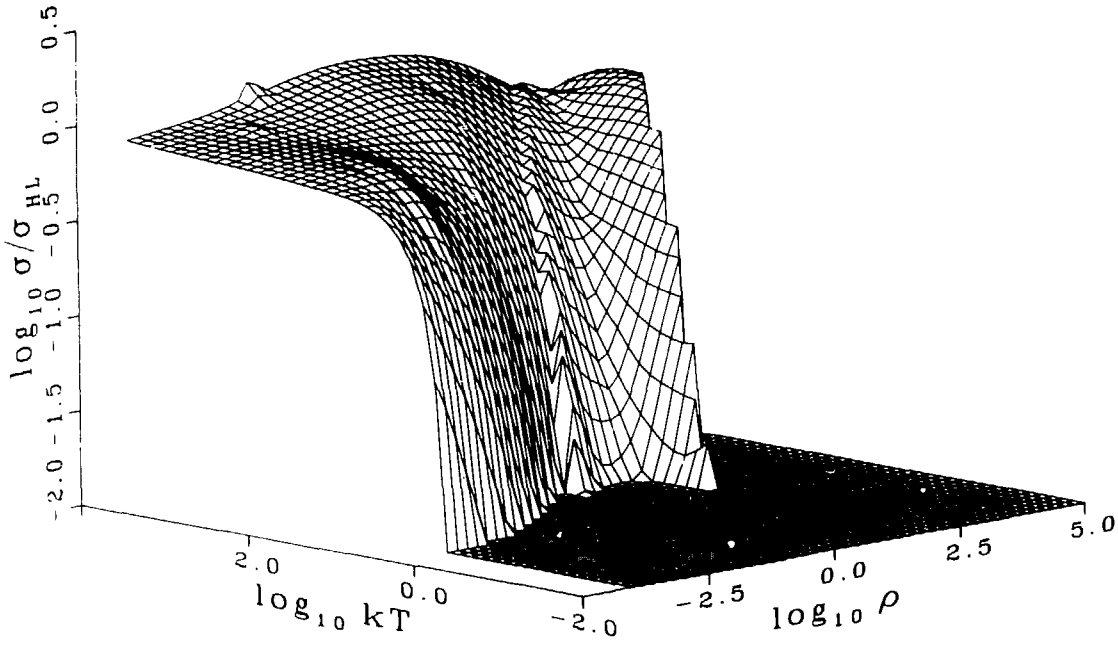

Fig. 27.
Comparison of calculated electrical conductivity σ with the method of Hubbard and Lampe σ_{HL}, for hydrogen as a function of temperature and density.

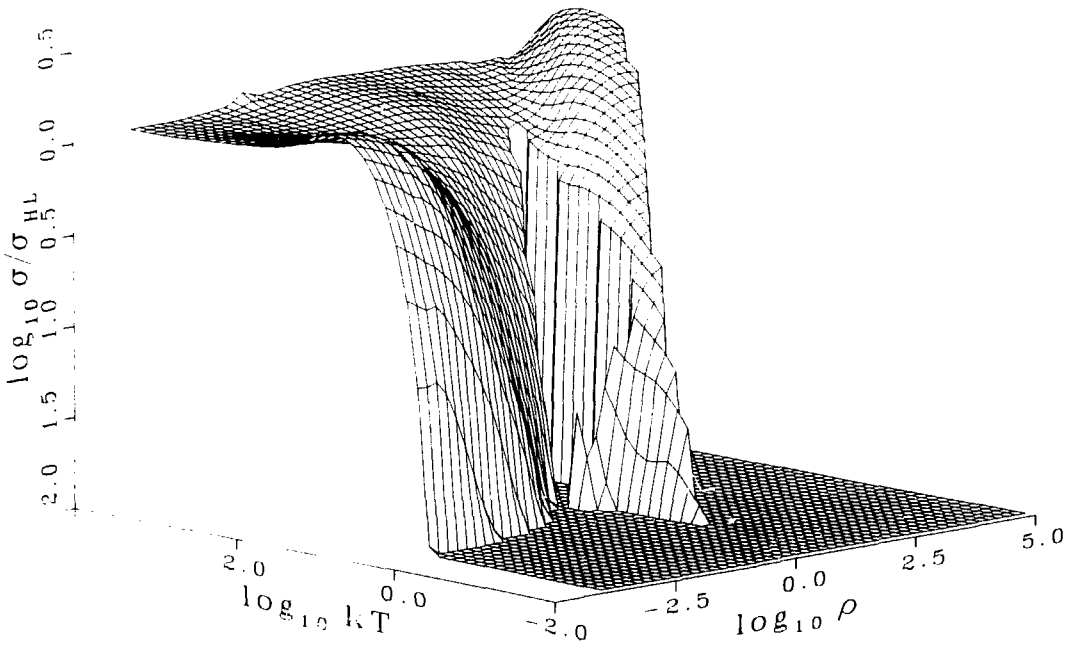

Fig. 28.
Comparison of calculated electrical conductivity σ with the method of Hubbard and Lampe σ_{HL}, for C_2H_3 as a function of temperature and density.

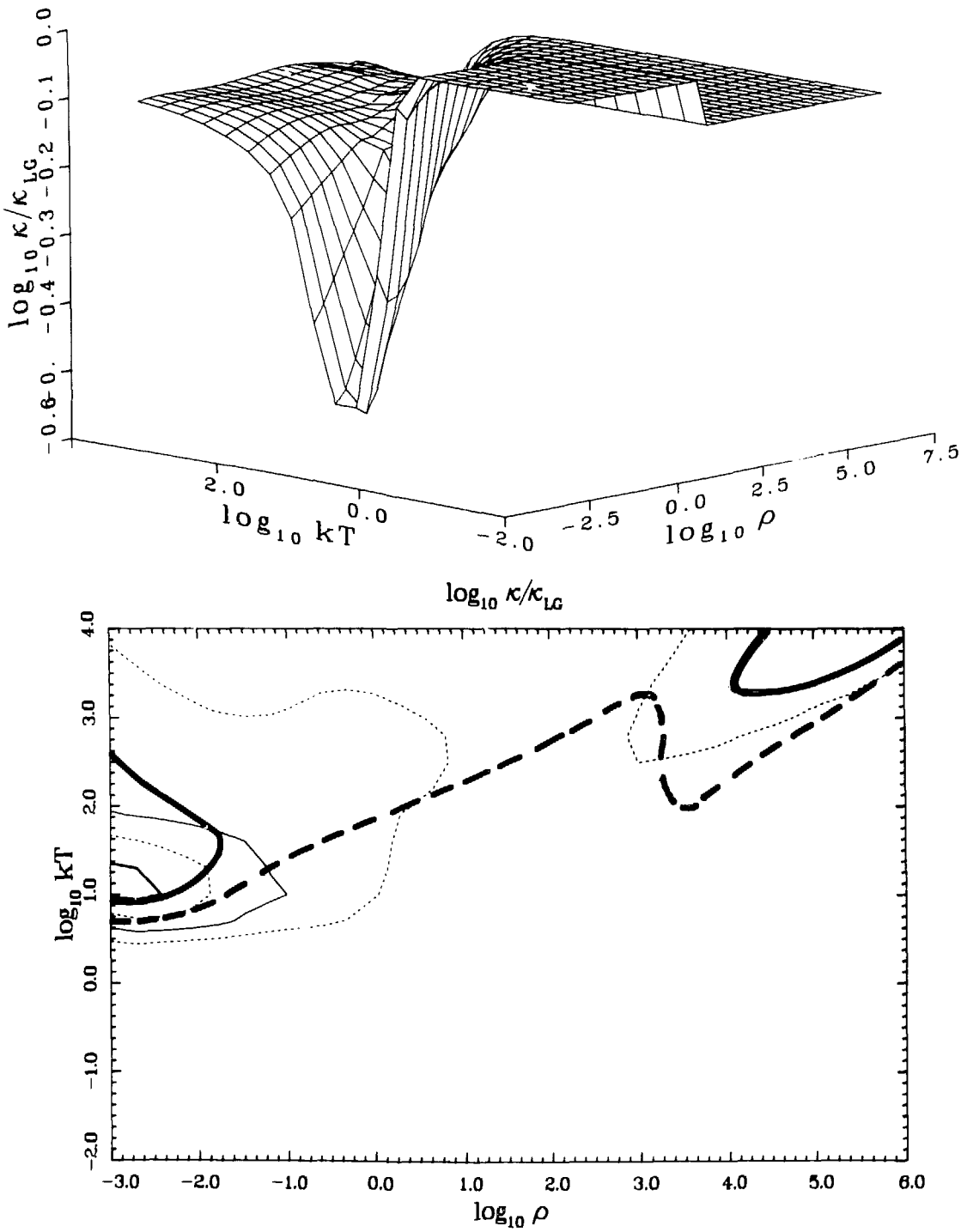

Fig. 29.
Comparison of calculated thermal conductivity κ with the degenerate Lorentz gas κ_{LG}, for carbon as a function of temperature and density. The heavy solid line represents the contour $\sigma=\sigma_{HL}$, and the heavy dashed line, the contour $\sigma=0.3\sigma_{HL}$.

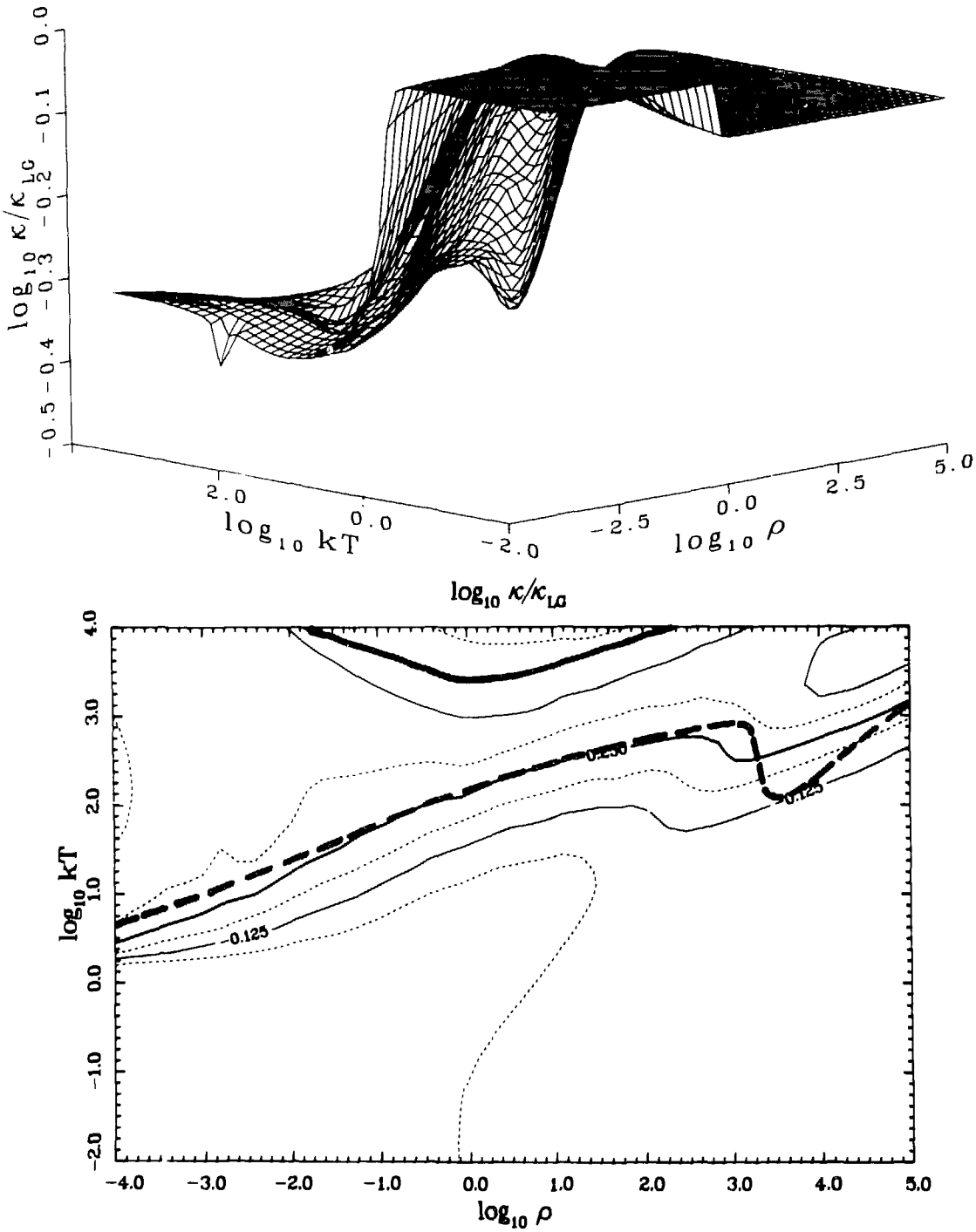

Fig. 30.
Comparison of calculated thermal conductivity κ with the degenerate Lorentz gas κ_{LG}, for hydrogen as a function of temperature and density. The heavy solid line represents the contour $\sigma=\sigma_{HL}$, and the heavy dashed line, the contour $\sigma=0.3\sigma_{HL}$.

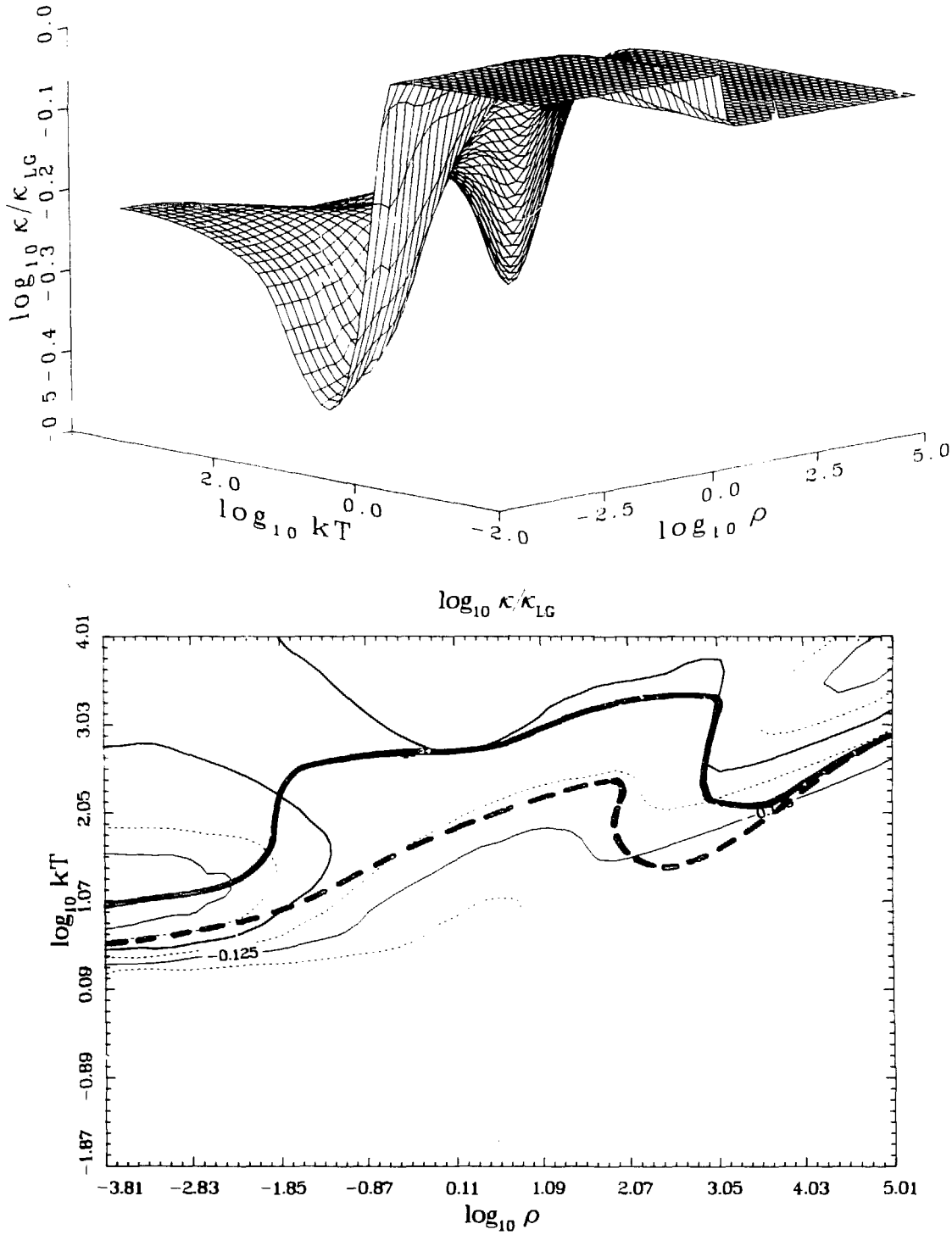

Fig. 31.
Comparison of calculated thermal conductivity κ with the degenerate Lorentz gas κ_{LG}, for C_2H_3 as a function of temperature and density. The heavy solid line represents the contour $\sigma=\sigma_{HL}$, and the heavy dashed line, the contour $\sigma=0.3\sigma_{HL}$.

REFERENCES

1. G. A. Rinker, Phys. Rev. B 31, 4207 (1985).

2. G. A. Rinker, Phys. Rev. B 31, 4220 (1985).

3. G. Rinker, Los Alamos National Laboratory report LA-9872-MS (January 1984).

4. G. Rinker, Los Alamos National Laboratory report LA-10202-MS (October 1984).

5. G. Rinker, Los Alamos National Laboratory report LA-10404-MS (May 1985).

6. F. J. Rogers, D. A. Young, H. E. DeWitt, and M. Ross, Phys. Rev. A 28, 2990 (1983).

7. M. Lampe, Phys. Rev. 170, 306 (1968); 174, 276 (1968).

8. W. B. Hubbard and M. Lampe, Astrophys. J. Suppl. Ser. 18, 297 (1969).

9. R. Landauer, J. Appl. Phys. 23, 779 (1952).

10. R. S. Hawke, T. J. Burgess, D. E. Duerre, J. G. Huebel, R. N. Keeler, H. Klapper, and W. C. Wallace, Phys. Rev. Letters 41, 994 (1978).